Anatomy of Rifting: Tectonics and Magmatism in Continental Rifts,
Oceanic Spreading Centers, and Transforms themed issue

Structural controls on fluid pathways in an active rift system: A case study of the Aluto volcanic complex

William Hutchison[1,*], Tamsin A. Mather[1], David M. Pyle[1], Juliet Biggs[2], and Gezahegn Yirgu[3]
[1]*COMET, Department of Earth Sciences, University of Oxford, South Parks Road, Oxford OX1 3AN, UK*
[2]*COMET, School of Earth Sciences, University of Bristol, Wills Memorial Building, Queens Road, Bristol BS8 1RJ, UK*
[3]*School of Earth Sciences, Addis Ababa University, P.O. Box 1176, Addis Ababa, Ethiopia*

ABSTRACT

In volcanically and seismically active rift systems, preexisting faults may control the rise and eruption of magma, and direct the flow of hydrothermal fluids and gas in the subsurface. Using high-resolution airborne imagery, field observations, and CO_2 degassing data on Aluto, a typical young silicic volcano in the Main Ethiopian Rift, we explore how preexisting tectonic and volcanic structures control fluid pathways and spatial patterns of volcanism, hydrothermal alteration and degassing. A new light detection and ranging (lidar) digital elevation model and evidence from deep geothermal wells show that the Aluto volcanic complex is dissected by rift-related extensional faults with throws of 50–100 m. Mapping of volcanic vent distributions reveals a structural control by either rift-aligned faults or an elliptical caldera ring fracture. Soil-gas CO_2 degassing surveys show elevated fluxes (>>100 g m^{-2} d^{-1}) along major faults and volcanic structures, but significant variations in CO_2 flux along the fault zones reflect differences in near-surface permeability caused by changes in topography and surface lithology. The CO_2 emission from an active geothermal area adjacent to the major fault scarp of Aluto amounted to ~60 t d^{-1}; we estimate the total CO_2 emission from Aluto to be 250–500 t d^{-1}. Preexisting volcanic and tectonic structures have played a key role in the development of the Aluto volcanic complex and continue to facilitate the expulsion of gases and geothermal fluids. This case study emphasizes the importance of structural mapping on active rift volcanoes to understand the geothermal field as well as potential volcanic hazards.

*Corresponding author; william.hutchison@earth.ox.ac.uk.

INTRODUCTION

Existing fault structures can play a significant role in the development of a volcanic complex, ultimately providing high permeability pathways for magma, hydrothermal fluids, and gas to ascend to the surface (e.g., Arnórsson, 1995; Rowland and Sibson, 2004; Caliro et al., 2005; Fridriksson et al., 2006). Understanding how preexisting structures such as regional tectonic faults and caldera ring faults affect fluid flow to the surface is a major task in defining the evolution of rift zones and has important implications for mineralization, geothermal exploration, and the assessment of volcanic hazard.

Recent work, specifically focused on hydrothermal venting and volcanic degassing (Schöpa et al., 2011; Pantaleo and Walter, 2013), has shown that while preexisting structures may control permeability at the edifice scale, at smaller scales these structural controls may be obscured by localized near-surface permeability variations. These local influences may include (1) lithological variations, where fluids will preferentially migrate along high permeability layers (e.g., poorly consolidated tephra layers) and (2) topographic controls, where the stress field induced by gravitational loading causes fracturing parallel to topography, and focuses pathways for steam and other gases toward topographic highs (Schöpa et al., 2011). To understand how large-scale structures influence active volcanic processes it is useful to look at the surface expression of different volcanic fluids (i.e., magma, hydrothermal fluids, and gas) across a variety of scales to disentangle large-scale structural controls from these localized near-surface permeability variations.

Both direct and remote measurements can be used to assess the spatial distribution of fluids and fluid pathways. Remotely sensed data such as lidar (light detection and ranging) and aerial photography (e.g., Pyle and Elliott, 2006; Cashman et al., 2013) are powerful tools to analyze volcano morphology, map sites of eruption and extrusion, and distinguish zones of hydrothermal alteration and fluid upwelling (e.g., Crowley and Zimbelman, 1997). On the other hand, volcanic gases (e.g., CO_2) that may be difficult to detect remotely, can be readily measured in the field using modern surveying techniques (Chiodini et al., 1998) and gridded to produce detailed maps of gas flux across a volcanic edifice (Cardellini et al., 2003; Parks et al., 2013). These techniques allow us to build detailed pictures of how different fluids are released from active volcanoes; the challenge for volcanologists is integrating these observations to unravel the subsurface structure and the processes controlling fluid pathways.

The Main Ethiopian Rift (MER, East Africa) provides an ideal natural laboratory to study how preexisting structural features (of both volcanic and tectonic origin) influence active volcanic processes. Firstly, the MER hosts a number of young silicic peralkaline volcanoes, allowing investigation of active magmatic and geothermal systems. Secondly, extension in the MER has generated abundant faults and fracture networks (e.g., Keir et al., 2006; Corti, 2009) through which magma can ascend and erupt. Finally, many of the MER volcanoes have undergone caldera collapse (Cole et al., 2005) and thus are likely to have established ring fault systems (Cole, 1969; Gibson, 1970; Mohr et al., 1980; Acocella et al., 2003; Rampey et al., 2010).

The silicic peralkaline volcanoes of the MER are among the least studied on Earth: few have detailed geological maps and significant knowledge gaps exist regarding their past and current activity (Aspinall et al., 2011). Detailed studies of peralkaline volcanic systems are limited to a few key complexes (e.g., Pantelleria; Mahood and Hildreth, 1983, 1986; Civetta et al., 1988; White et al., 2009; Neave et al., 2012; Williams et al., 2013), despite the fact that they appear

Geosphere; June 2015; v. 11; no. 3; p. 542–562; doi:10.1130/GES01119.1; 12 figures; 2 tables.
Received 18 August 2014 ♦ Revision received 14 December 2014 ♦ Accepted 9 February 2015 ♦ Published online 2 April 2015

to be a ubiquitous feature of continental rift zones (Mahood, 1984; Cole et al., 2005). The caldera structures produced at peralkaline volcanic centers in the East African Rift system are also of note because many appear elliptical in map view (e.g., Acocella et al., 2003; Bosworth et al., 2003; Holohan et al., 2005). While several recent publications have emphasized the role of elongate magma chamber collapse in generating elliptical calderas in the East African Rift system (e.g., Acocella et al., 2003; Bosworth et al., 2003), there is a lack of consensus regarding the exact mechanism in the MER. Establishing the controls on magma rise and ponding in tectonically thinned crust is fundamental to understanding how continental rift zones evolve (Ebinger et al., 2010).

In this paper we integrate observations from field campaigns, airborne remote sensing (lidar, aerial photos) and soil-gas CO_2 surveys to examine how magma, hydrothermal fluid, and gas pathways are coupled to the major structural features on Aluto, a typical young peralkaline volcanic complex of the MER. We show that each data set provides unique information about the complex and the links between volcanic activity and preexisting volcanic and tectonic structures. From these data we develop a conceptual model that captures both the volcanic evolution and the role these major structures play in controlling fluid pathways.

MER—REGIONAL SETTING

The MER (Fig. 1) is a zone of active extension in the East African Rift system that connects the Afar depression to the north with the Turkana depression and Kenyan rift to the south. The MER is an oblique rift, exhibiting an overall NE–SW trend, formed by E–W extension between the Nubia and Somalia plates via both magmatic intrusion and tectonic faulting (Ebinger, 2005; Corti, 2009; Corti et al., 2013a). Geodetic and seismic data (Bendick et al., 2006; Keir et al., 2006; Stamps et al., 2008) indicate that the current E–W (~N100°E) extension rates are 4–6 mm yr^{-1}. The MER is usually divided into three sectors (northern, central, and southern) that reflect differences in terms of the spatial pattern of the faulting (Agostini et al., 2011), the timing of the major faulting episodes (Woldegabriel et al., 1990; Wolfenden et al., 2004; Bonini et al., 2005), and the thermal-mechanical state of the lithosphere (e.g., Keranen and Klemperer, 2008). This pattern is consistent with rift maturity increasing northward along the MER toward Afar, where the overall physiology changes from continental rifting to incipient oceanic spreading (Beutel et al., 2010; Ebinger et al., 2010; Ferguson et al., 2013).

The MER has two distinct fault sets: (1) NE–SW-oriented border faults with large vertical offsets (>100 m) on the boundaries of the rift, and (2) a set of closely spaced internal faults, the Wonji faults, with smaller vertical offsets (<100 m) oriented NNE–SSW and concentrated on the rift floor (Chorowicz et al., 1994; Boccaletti et al., 1998). In the central MER (CMER), the focus of this paper, the border faults formed at 6–8 Ma (Woldegabriel et al., 1990; Bonini et al., 2005), while the Wonji faults initiated ca. 2 Ma (Boccaletti et al., 1998; Ebinger and Casey, 2001). These observations support models of rift initiation and continental extension (Hayward and Ebinger, 1996; Ebinger, 2005; Corti, 2008) whereby border faults are progressively abandoned and strain becomes localized to active segments central to the rift zone. This focusing of strain has resulted in discrete narrow zones (~20 km wide) where extension is accommodated by Wonji faults as well as magmatic intrusion (Keranen et al., 2004; Keir et al., 2005; Kendall et al., 2005; Mackenzie et al., 2005). In the CMER, while the border faults are still seismically active (Keir et al., 2006; Pizzi et al., 2006) much of the active tectonic deformation occurs in the magmatic segments via the NNE–SSW Wonji faults (Keir et al., 2006).

Magmatic intrusion within the active segments has produced abundant surface volcanism. Basalts are associated with scoria cones and eruptive fissures, whereas rhyolitic volcanism has produced a series of peralkaline volcanoes comprising silicic lava flows, domes, and coulees, and extensive pyroclastic products (Gibson, 1969; Di Paola, 1972).

Aluto Volcano—Geological Overview and Deep Well Observations

Aluto is a silicic peralkaline volcano located in the CMER (Fig. 1). The complex (outlined by the white box in Fig. 1 and detailed in Fig. 2A) is dominated by an ~14-km-wide, 700-m-high edifice composed of a thick pile of coalescing rhyolitic lava flows and domes, pumice cones, and ignimbrite deposits. There are a significant number of smaller volcanic vents and domes formed off the main edifice, particularly to the northwest of the complex. Aluto has an internally drained central depression (herein referred to as a caldera floor) that has been partially in-filled by alluvium and reworked material from the surrounding surface volcanic deposits. While there are no detailed accounts of the eruptive history of the complex, descriptions of the geology of Aluto are in regional-scale mapping reports (e.g., Dakin and Gibson, 1971; Di Paola, 1972; Kebede et al., 1985); studies of the Ziway-Shala lake basin system (Gasse and Street, 1978; Street, 1979; Le Turdu et al., 1999; Benvenuti et al., 2002; Gibert et al., 2002), and publications related to geothermal development on Aluto (Gebregzabher, 1986; Valori et al., 1992; Gizaw, 1993; Gianelli and Teklemariam, 1993; Teklemariam et al., 1996; Saibi et al., 2012). This work and our own field investigations suggest that the Aluto volcanic complex has undergone several cycles of explosive and effusive volcanism throughout its history and that these eruptive phases have been dominantly silicic in composition.

There are few constraints on the ages of the erupted products of Aluto. A single K/Ar date from a geothermal feasibility study gives an age of 155 ± 8 ka for the Hulo-Seyno ignimbrite, which is taken as one of the first products of the silicic complex (ELC Electroconsult, 1986). The most recent volcanic activity on Aluto is represented by a series of obsidian lava flows, the youngest of which likely erupted within the past 2000 yr (Gianelli and Teklemariam, 1993). Aluto is an active volcanic system. Across the complex, hydrothermal manifestations include fumaroles and hot springs (Kebede et al., 1985). Interferometric synthetic aperture radar (InSAR) studies show that Aluto has undergone several uplift and subsidence events of 10–15 cm over the past decade (Biggs et al., 2011). While the exact mechanism driving deformation is uncertain, the source characteristics and time scale are indicative of shallow magmatic processes active beneath the complex (Biggs et al., 2011).

Eight exploration wells have been drilled on Aluto (LA-1–LA-8; Fig. 2A). From these a deep stratigraphy of Aluto has been assembled that forms the model for the geothermal field (Gizaw, 1993; Gianelli and Teklemariam, 1993). A geological cross section compiled from these previous studies, as well as various drilling reports provided by the Geological Survey of Ethiopia, is given in Figure 2B. The deep well stratigraphy reveals that there are substantial offsets in the units between the wells. This is taken as evidence that faults, shown in Figure 2A, dissect the complex. There are also thickness variations within individual units between the wells; this is particularly evident in a Pleistocene lacustrine horizon that shows a stepped thinning pattern from west to east (i.e., from the rift center, toward the rift margin). The abrupt changes in thickness of this unit suggest that deposition took place on an uneven surface. Given the rift geological setting, this is likely to be associated with faulting; however, other processes such as wedging out of the layer on a previous erosive surface cannot be ruled out. The Pleistocene lacustrine horizon predates the Aluto silicic products, so if deposition of this unit was fault controlled this would imply that

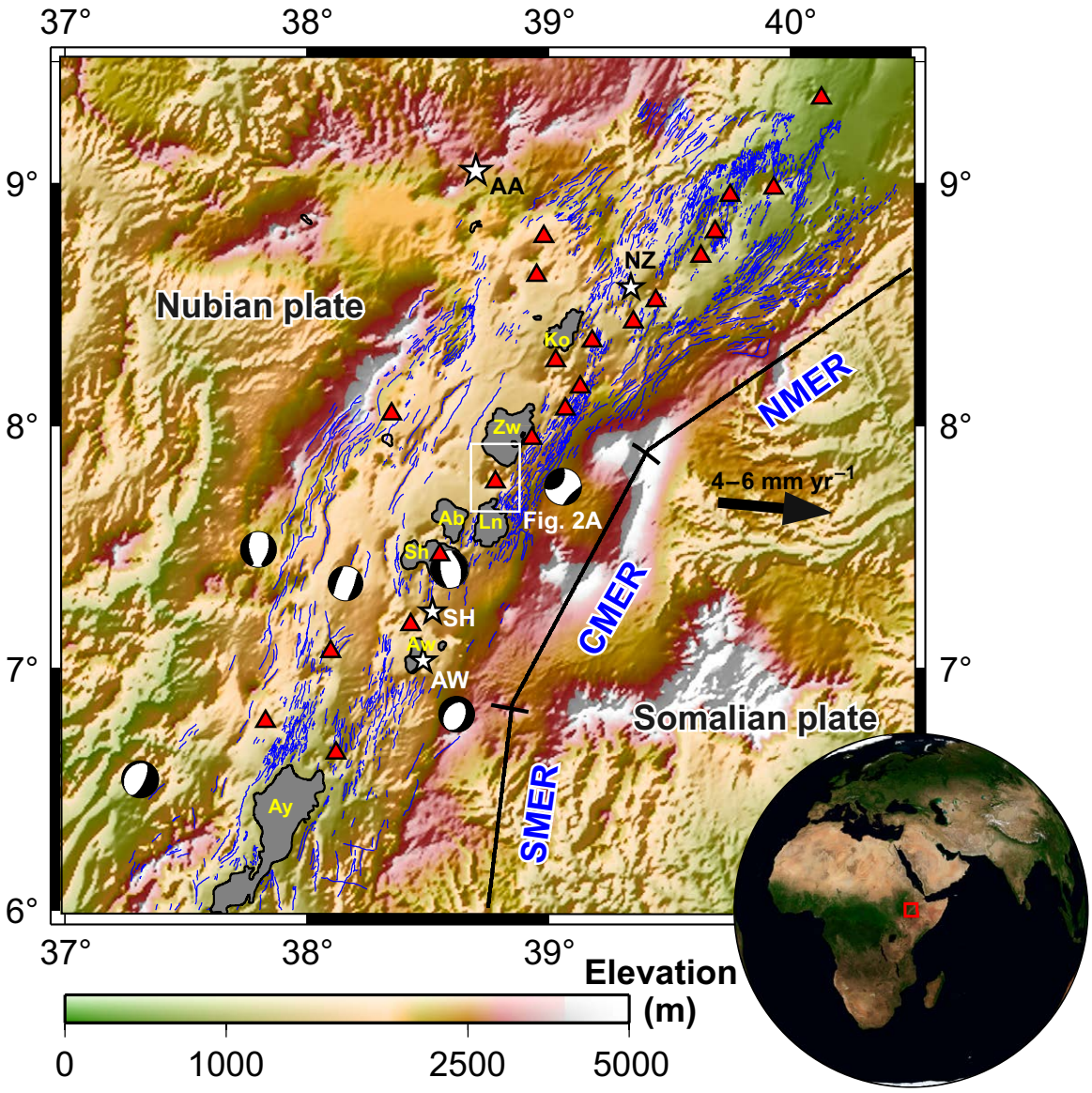

Figure 1. Topographic map of the Main Ethiopian Rift (MER) indicating the three main sectors (northern, central and southern, i.e., NMER, CMER, and SMER). The surface faults (mapped by Agostini et al., 2011) are shown in blue. Earthquake locations and focal mechanisms for the region are from the Global Centroid Moment Tensor Project catalogue (http://www.globalcmt.org; 1976–2012; M > 5). Red triangles identify volcanic centers thought to have been active in the Holocene (Siebert and Simkin, 2002). White stars identify major centers of population (after the Socioeconomic Data and Applications Center, http://sedac.ciesin.columbia.edu/): AA—Addis Ababa; NZ—Nazareth; SH—Shashemene; AW—Awassa. Lakes outlined in the MER: Ko—Lake Koka; Zw—Lake Ziway; Ln—Lake Langano; Ab—Lake Abijta; Sh—Lake Shala; Aw—Lake Awasa; Ay—Lake Abaya. The Aluto volcanic complex is located within the white rectangle (Fig 2A).

significant faulting preceded volcanic activity at Aluto. Of the 8 wells drilled, only 2 (LA-3 and LA-6) are productive. The sustained production in these wells is linked to their location along a major NNE–SSW fault on Aluto (herein referred to as the Artu Jawe fault zone; AJFZ in Fig. 2A). Well temperatures (Gizaw, 1993), alteration mineral assemblages (Gebregzabher, 1986; Gianelli and Teklemariam, 1993), and the Na/K ratio of geothermal fluids from these deep wells (Gizaw, 1993) all support the hypothesis that this faulted zone, photographed in Fig. 3A, is the main upflow zone through which high-temperature fluids ascend to the surface.

METHODS

Remote Sensing

Mapping of the volcanic and tectonic landforms on Aluto was carried out using airborne and satellite remote sensing, complemented by eight weeks of field mapping to ground truth these interpretations. High-spatial-resolution topography and imagery of the volcanic edifice were acquired in November 2012 by the UK Natural Environmental Research Council's Airborne Research and Survey Facility. The aircraft was equipped with a Leica ALS50 airborne laser scanner, AISA (Airborne Imaging Spectrometer for Application) Eagle and Hawk hyperspectral instruments and a Leica RCD105 39 megapixel digital camera. The lidar system acquired first,

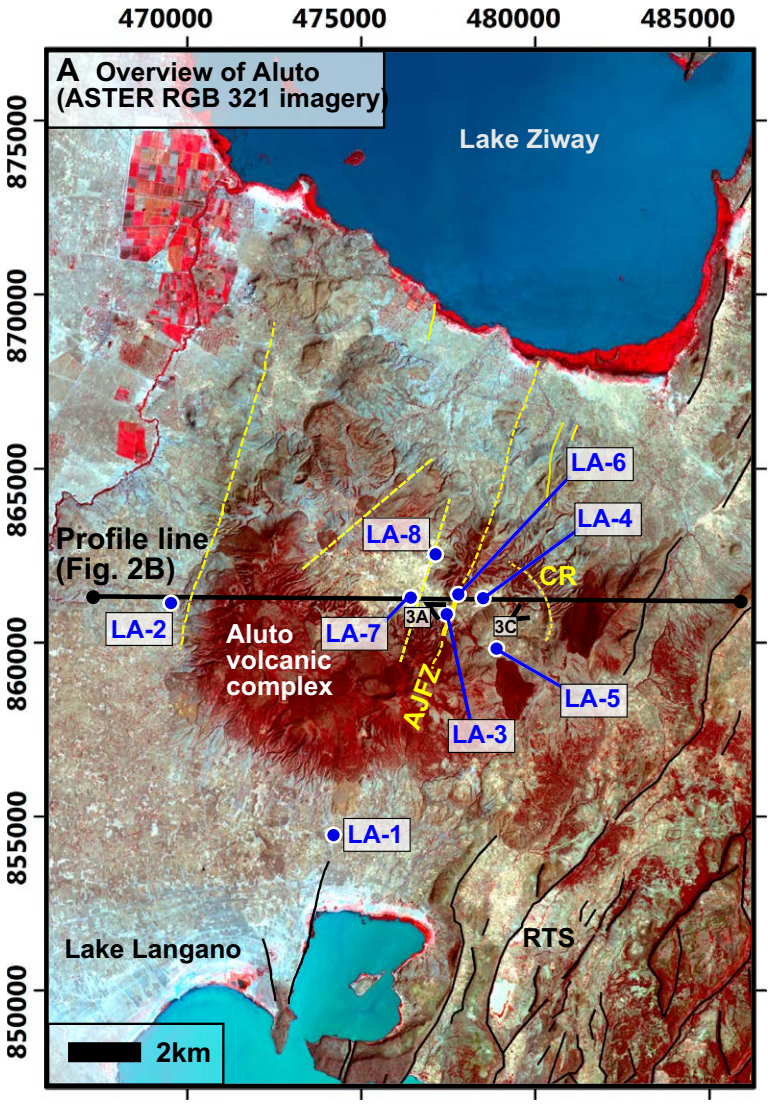

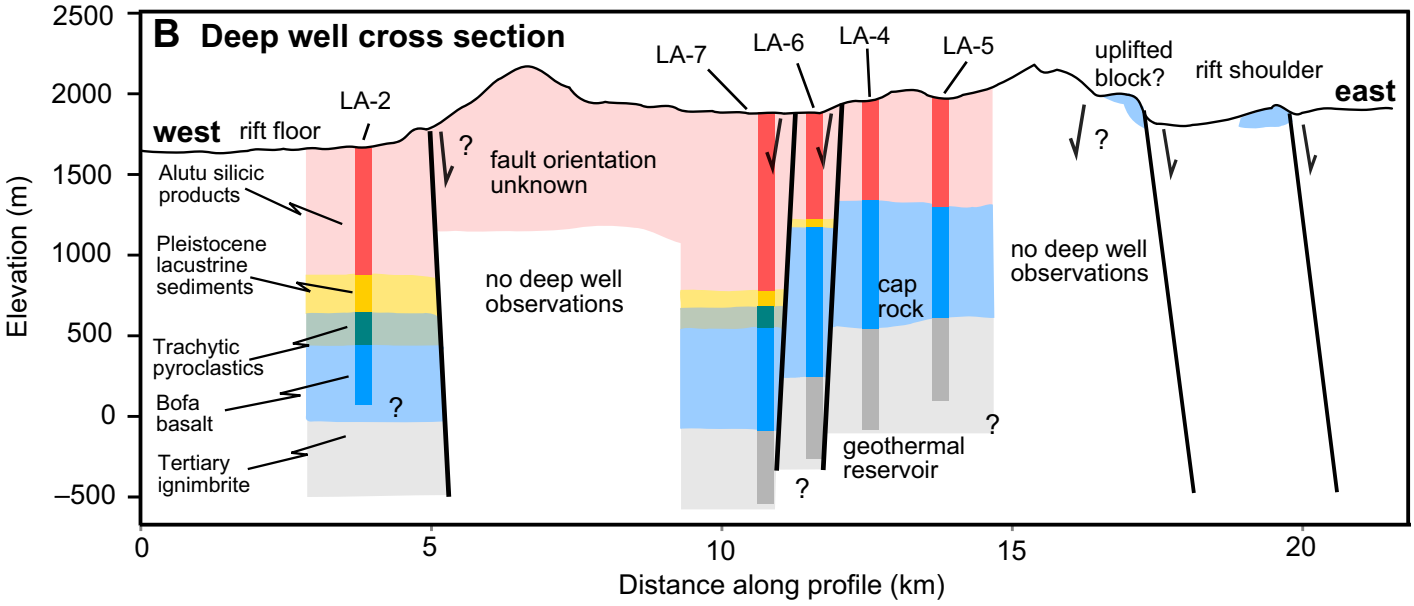

Figure 2. (A) ASTER (Advanced Spaceborne Thermal Emission and Reflection Radiometer) RGB321 image of Aluto volcano and the surrounding area. Geothermal wells on Aluto are labeled in blue (only wells LA-3 and LA-6 are productive). Yellow lines indicate the location of faults mapped in previous studies (Kebede et al., 1985; ELC Electroconsult, 1986) or indicated by deep well data (in B). Black open arrowheads or view lines indicate viewing direction for photographs in Figure 3. Coordinates are in UTM (Universal Transverse Mercator) Zone 37N, with the WGS84 (World Geodetic System 1984) datum (for this figure as well as all subsequent maps). AJFZ—Artu Jawe fault zone; RTS—regional tectonic structures visible east of Aluto; CR—caldera rim. (B) West-east cross section showing the deep stratigraphy and hypothesized subsurface structure. Well data represent the synthesis of several publications (Gizaw, 1993; Gianelli and Teklemariam, 1993; Teklemariam et al., 1996) and drilling reports provided by the Geological Survey of Ethiopia (Yimer, 1984; Mamo, 1985; ELC Electroconsult, 1986; Teklemariam, 1996). The geological units shown have been correlated between the different wells on Aluto (Gizaw, 1993; Gianelli and Teklemariam, 1993) and indicate a prevailing mode of deposition rather than a single homogeneous unit (e.g., paleosols occur within the Bofa basalt and ash horizons occur within lacustrine sequences). The section line is shown in A. Note also that data from well LA-5 have been collapsed onto the section line.

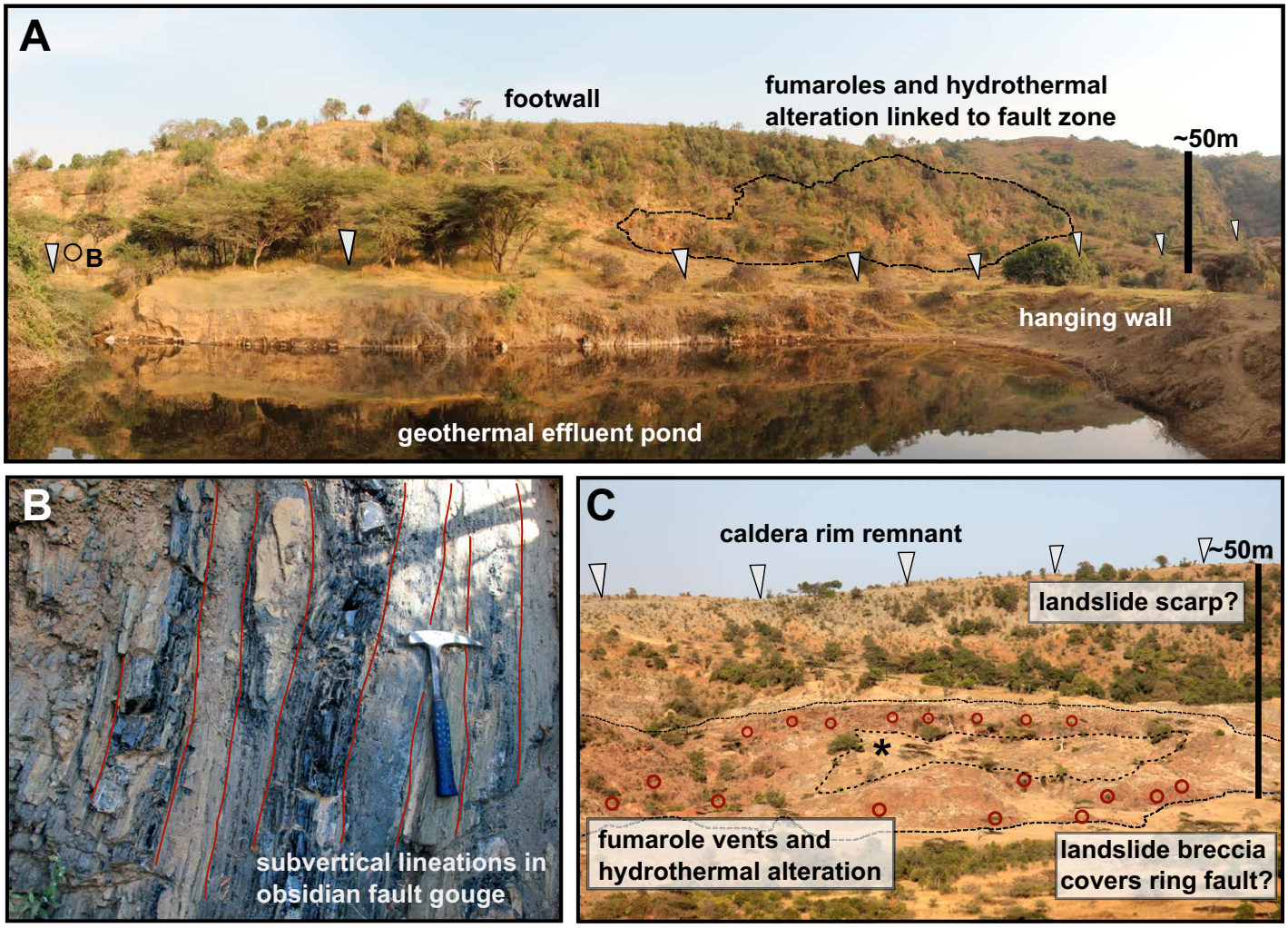

Figure 3. Photographs of major volcanic and tectonic structures on Aluto. (A) The Artu Jawe fault scarp viewed from the west (located in Fig. 2A). Along the escarpment fumaroles are visible at the base of the structure and there is evidence of hydrothermal alteration at the surface. (B) Subvertical foliations developed in obsidian in crush zone of Artu Jawe fault scarp (located in A). Hammer is 30 cm in length. (C) The caldera wall of Aluto, identifying fumarole vents (red circles) and hydrothermal alteration at the base of the structure. Asterisk in the center of the fumarole field indicates a zone that does not show any surface alteration and has low ground temperatures and CO_2 gas flux relative to the surroundings (see text).

second, and last returns for ~140 × 10^6 discrete points and was operated with a pulse repetition frequency of 46,200 kHz and scan frequency of 29.9 Hz. The last-return data points were combined into a single point cloud and a 2-m-resolution digital elevation model (DEM) was generated using GRASS (Geographic Resources Analysis Support System; http://grass.osgeo.org/). The DEM was also used to orthorectify aerial photos acquired by the digital camera. Orthorectification was performed with the Leica Photogrammetry Suite in ERDAS Imagine software (www.hexagongeospatial.com/products/remote-sensing/erdas-imagine) using camera calibration information provided with the photographic data. Orthophotos reveal valuable surface and morphological information and have a resolution of 0.25–0.50 m.

Using the airborne data we mapped (1) volcanic vent locations, the site of an effusive vent of a lava flow, and the center of a crater (or set of nested crater features), represented by points (Figs. 4 and 5), and (2) volcanic lineaments, crater rims, and other linear fissures represented by line features (Fig. 5B). We could only map volcanic lineaments on the main edifice of Aluto (i.e., the area covered by the lidar DEM); off the main edifice, Google Earth and ASTER (Advanced Spaceborne Thermal Emission and Reflection Radiometer) satellite imagery were used. Owing to their lower resolution and the generally greater erosion of the volcanic landforms beyond the main edifice, only vent locations could be accurately mapped (Fig. 4).

The spatial distribution of volcanic vents and the orientation of elongate vents and fissures can be used to make inferences about geometry of feeder dikes and ultimately evaluate the underlying structural or stress field controls on magma pathways (e.g., Nakamura, 1977; Tibaldi, 1995; Paulsen and Wilson, 2010). On the main edifice, we used crater rim and fissure line data (Fig. 5) to investigate whether these features exhibited any prevailing orientations and alignments with regional faults. To do this we analyzed the orientation of all individual segments of the digitized crater and fissure line data and length-weighted our results. The

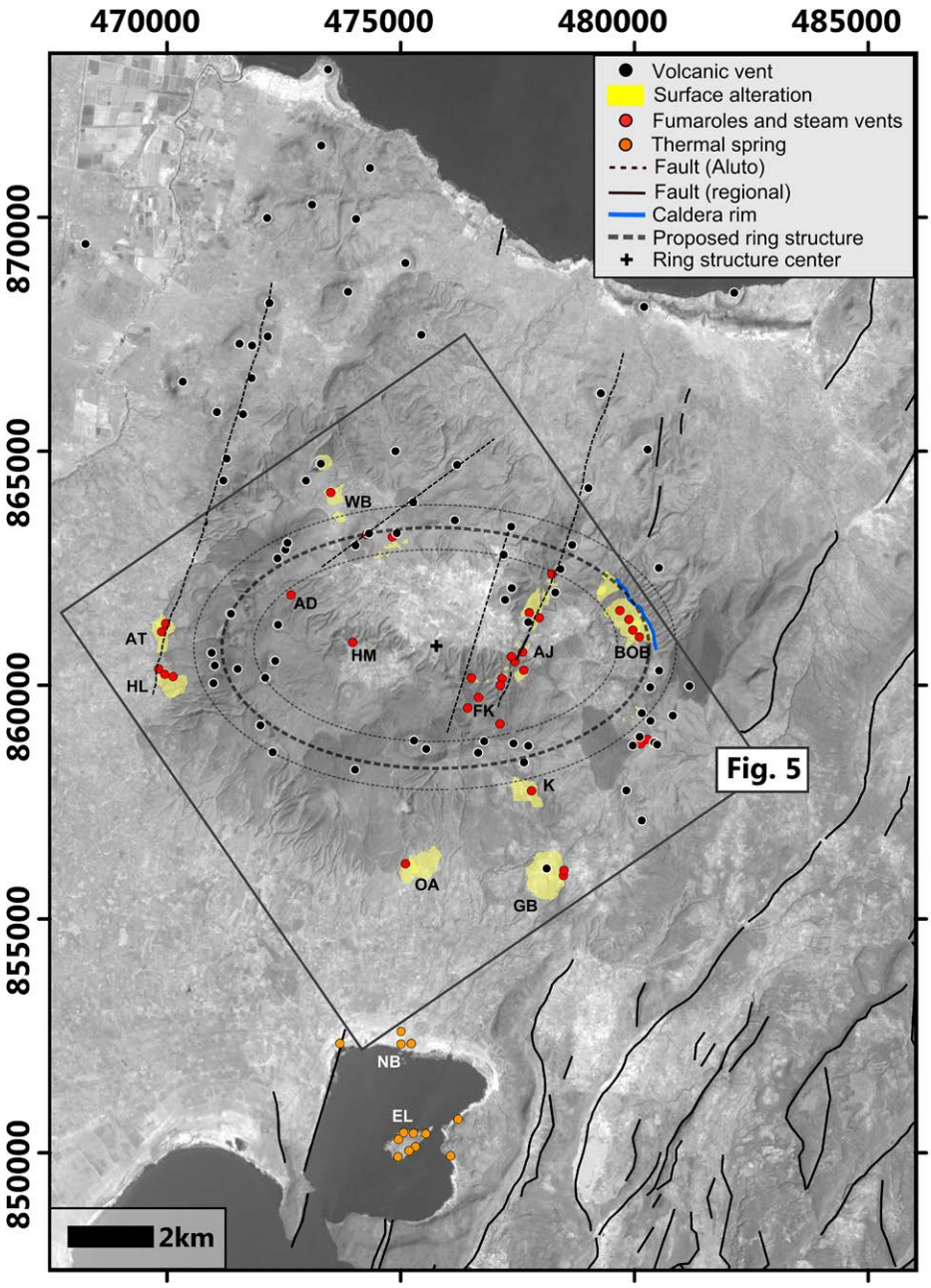

Figure 4. Map of volcanic vents, hydrothermal alteration, active fumaroles, and hot springs in the Aluto volcanic complex. Faults on the complex have either been mapped using remote sensing data sets (this study) or have been suggested by previous geological mapping reports and deep well data (Kebede et al., 1985; ELC Electroconsult, 1986; Gizaw, 1993; Gianelli and Teklemariam, 1993). Regional faults were mapped by Agostini et al. (2011). The dashed ellipses show the size and orientation of a buried ring fault that we propose may explain the distribution of volcanic vents on the main edifice; the fine dashed ellipses represent ±500 m uncertainty bounds on the central ellipse. The mapped caldera rim overlaps the proposed ring structure. Major hydrothermal zones are labeled and link to the summary in Table 1, where the abbreviations used in the figure are expanded.

results are illustrated for an individual elongate crater in Figure 6A; the inset clearly demonstrates a rose plot with prevailing E–W orientation. This method is similar to that employed previously (e.g., Trippanera et al., 2014), but has the advantage that rather than taking one averaged elongation direction, all mapped segments that make up the crater and fissures are used and can be compared together. Beyond the coverage of the lidar DEM, where it was not possible to carry out detailed volcanic lineament mapping, an azimuth-based method was used to assess vent alignments (Lutz, 1986; Wadge and Cross, 1988; Lutz and Gutmann, 1995; Cebriá et al., 2011). Vents are treated as discrete points, and the azimuth (or alignment direction) between a vent and its neighbors is determined for a given separation distance. When vent locations (or magma pathway to the surface) are controlled by faulting, then neighboring vents will have similar orientations relative to each other. However, as the distance between vents increases, then so does the likelihood that the vents will not be located on the same fracture. Thus, alignments need to be assessed within a specific separation window to best expose regional structural trends (Cebriá et al., 2011). Ultimately, these numerical interpretations of the volcanic vents and structural data are considered in the context of the physical observations from the remote sensing, field observations, and the CO_2 degassing measurements to assess their real geological significance.

Hydrothermal fluid upwelling on Aluto causes visible alteration of the surface volcanic products, producing red and orange clays over areas >>10 m^2, which can be mapped using aerial photographs (Fig. 6B). While an automated mapping approach using the spectral signature of these alteration facies (e.g., Crowley and Zimbelman, 1997) would be feasible given our data set, for the purposes of this study the resolution of the aerial photos is sufficiently high that major altered zones can be approximately mapped, and their locations can be linked with structural interpretations and CO_2 degassing results. Our assessment of hydrothermal alteration made using the orthophotos correlates well with fumarole vents mapped on the ground by the Geological Survey of Ethiopia (Kebede et al., 1985); for hot spring locations that were beyond the coverage of our remote sensing data, we used Kebede et al. (1985) to constrain their location.

Soil CO_2 Flux

Measurements of soil CO_2 flux on Aluto were undertaken in three surveys between January 2012 and February 2014. The first survey (January 2012) sought to transect large-scale structures and identify whether they provided key permeability pathways for CO_2-rich geothermal fluids and magmatic gases to upwell. Degassing surveys were conducted

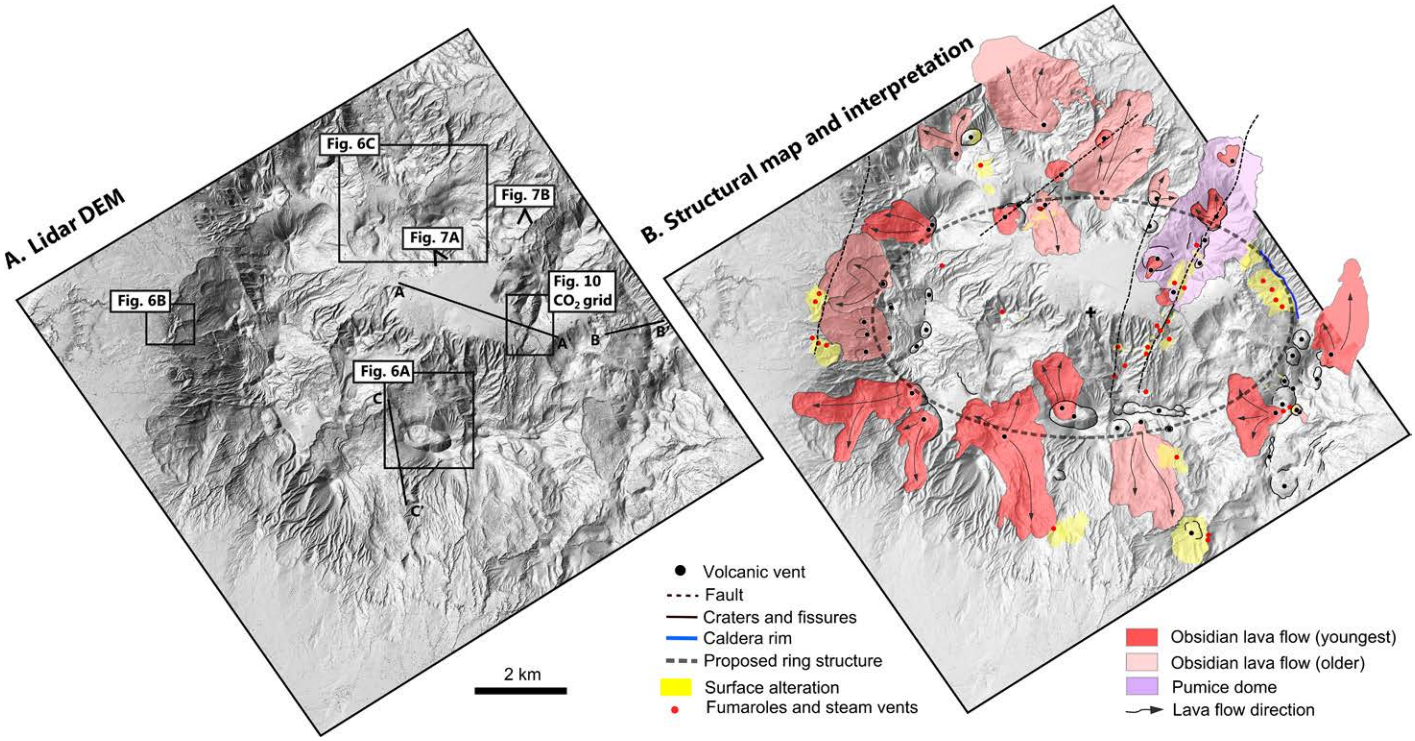

Figure 5. (A) Lidar hillshade DEM covering the main edifice of Aluto volcano (black box in Fig. 4). Black box insets link to Figures 6 and 10, where detailed imagery and interpretation of the volcanic features are given. Black triangular features show the viewing direction for the three-dimensional DEM imagery given in Figure 7. The light blue lines A–A′, B–B′, and C–C′ correspond to the CO_2 degassing transects given in Figure 9. (B) Structural map and interpretation of the DEM imagery. The older, more weathered obsidian lava flows of Aluto are covered in a thin shower of gray pumice, unlike the younger obsidian lavas. The lidar data set used in this study is doi:10.6084/m9.figshare.1261646.

in November 2012 and February 2014, and focused on producing a detailed map of spatial degassing patterns along the major tectonic fault (Artu Jawe fault zone). A 1000 m × 800 m study area (Fig. 5A) was chosen to include both the major fault scarp (photograph in Fig. 3A) and the productive geothermal wells (LA-3 and LA-6). A 30-m sampling grid was use, a compromise between attaining spatial coverage of the fault zone at sufficient sampling resolution. In total 560 sites were visited (424 in November 2012 and 136 in February 2014). Those that were in geothermal effluent ponds, areas of dense vegetation, or on hazardous slopes were excluded, and in some instances extra measurements were made off the predefined sampling grid to help characterize the highest values in the degassing regions.

The CO_2 flux was measured directly using two portable closed system gas analyzer units (a LICOR LI-8100 automated soil CO_2 flux system and a PP-systems SRC-1 chamber with EGM-4 analyzer). Both instruments have an infrared gas analyzer and use the accumulation method (Parkinson, 1981; Chiodini et al., 1998) to measure CO_2 flux. Measurements were consistent between the instruments; comparisons made at identical sites showed variations of 10%–25% between the two instruments (significantly less than the variation seen across the complex). Repeated site measurements showed variations of ~25% in low flux zones (<10 g m^{-2} d^{-1}) and <10% in high flux zones (>100 g m^{-2} d^{-1}), consistent with random error in natural emission rates (Carapezza and Granieri, 2004; Viveiros et al., 2010) and in line with the quoted reproducibility of each instrument (5%–10%, Chiodini et al., 1998; Giammanco et al., 2007).

To generate maps of soil CO_2 flux from the discrete point measurements the sequential Gaussian simulation (sGs) method was used (Cardellini et al., 2003). A simulation grid was defined (at higher spatial resolution than the sampling grid) and 100 sGs were performed using the sgsim code (Deutsch and Journel, 1998) available in the Stanford Geostatistical Modeling Software (SGeMS) open-source geostatistics package (Remy et al., 2009). A CO_2 flux map was constructed from these simulations taking the arithmetic mean of each individual cell across all simulations, equivalent to the E-type soil flux map proposed by Cardellini et al. (2003). The total CO_2 flux was calculated for each simulation and the mean and standard deviations of all simulations were computed and used to estimate total CO_2 release as well as the associated uncertainty (Cardellini et al., 2003).

RESULTS

Recent Volcanism and Links to a Ring Fracture System

The spatial distribution of volcanic vents on Aluto is shown in Figure 4. Vents are largely restricted to the main edifice and a NNE–SSE-trending zone to the northwest of this. A detailed map of volcanic vents, lava flows, craters and fissures overlain on the lidar DEM is given in Figure 5. Lava flows on the central edifice are rhyolitic; Figure 6A shows shaded relief and slope maps for a typical obsidian lava deposit. Craters are predominantly <1 km in diameter and <100 m deep; many are elliptical (e.g., Fig. 6A) or are composed of nested structures (Fig. 5).

On the northeast flank of Aluto, several lines of evidence support the existence of a caldera rim structure; from remote sensing data we identify a 2.5-km-long arcuate structure (CR in Fig. 2A; also see Figs. 4 and 5) that is orthogonal to

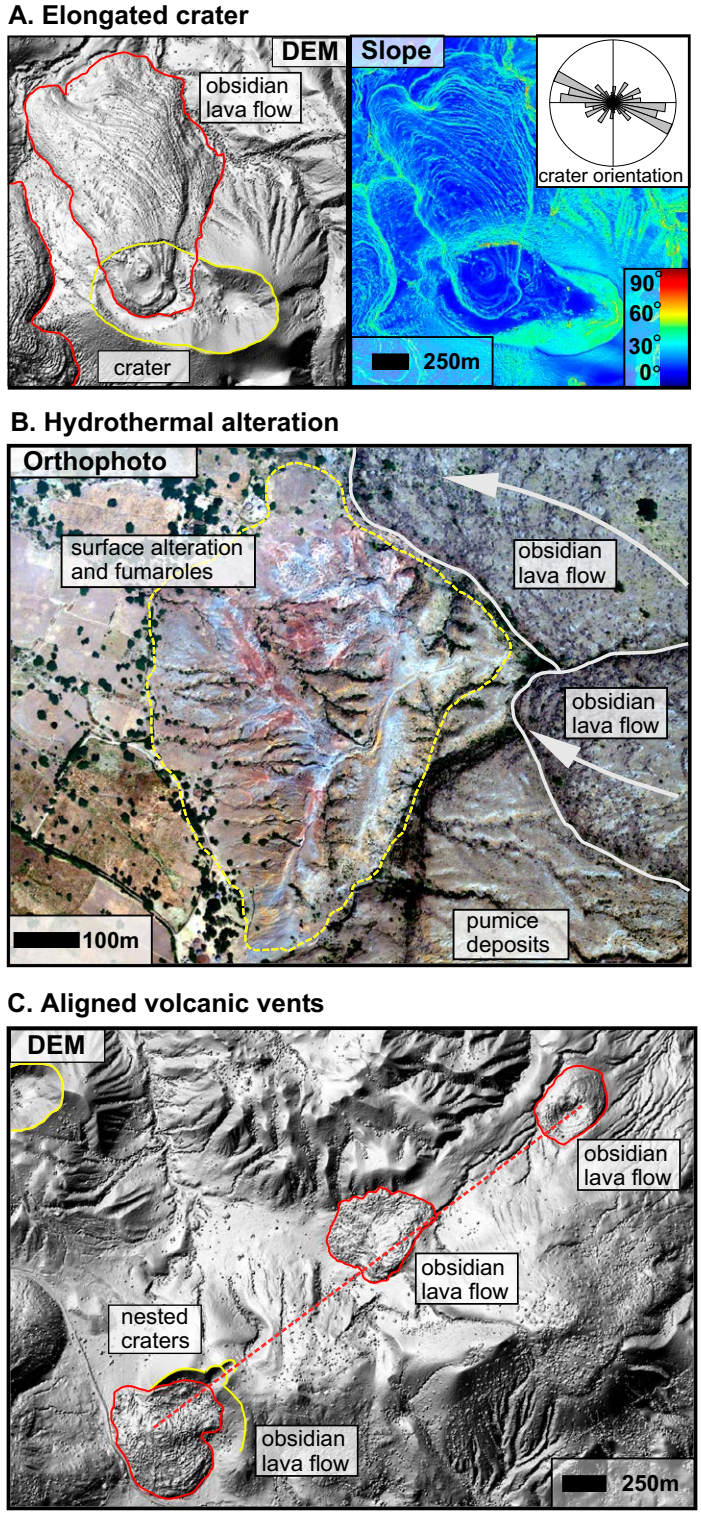

Figure 6. Examples of volcanic features mapped using the airborne data sets. (A) Hillshade DEM and slope map showing a typical obsidian lava flow vent and elongate crater. These flows often preserve compression folds on the surface that are characteristic of viscous silicic lavas (e.g., Fink, 1980; Gregg et al., 1998; Pyle and Elliott, 2006). The length-weighted rose diagram (top right) was generated by analyzing the orientation of all the individual segments that compose the crater feature (yellow outline); the dominant ESE–WNW orientation is clearly identified (for a circular crater rim, a radial distribution would be generated). (B) Aerial photograph of the Auto fumarole zone on the west of Aluto. Hydrothermal alteration of pumiceous deposits produces bright red clays adjacent to active fumaroles. (C) Hillshade DEM identifying a set of three aligned obsidian domes and nested craters on the west of the caldera floor suggestive of an underlying tectonic control.

the regional NNE–SSE tectonic structures (RTS in Fig. 2A). Viewed from the southwest (Fig. 3C), the rim comprises a steep wall 50–60 m in height. Fumaroles and hydrothermal alteration are picked out at the base of the structure (Fig. 3C), and tentatively correlated with a buried ring fault. Northeast of the rim (Figs. 2A and 5) the topography gently slopes away from the edifice and is incised by numerous gullies and channels. The morphology of this structure is characteristic of a volcanic caldera (Lipman, 1997; Cole et al., 2005), including a caldera rim, curving landslide scarp, and possible landslide breccia that conceals the ring fault (labeled in Fig. 3C).

An underlying caldera ring fault (E–W-oriented ellipse; Figs. 4 and 5) centered on the floor of the main edifice may explain a number of aspects of the young volcanism. Assuming that vent and fissure elongation parallels the orientation of subsurface fractures (Paulsen and Wilson, 2010), then crater rim and fissure lineations in Figure 5 can be used as proxy for the underlying structures feeding surface eruption. Vent elongations on the southern rim of Aluto show clear E–W orientations (e.g., Fig. 6A, and the nested crater structures east of this in Fig. 5B) indicative of an E–W–oriented fissure feeding surface eruptions. In Figure 5B it is also clear that mapped crater rims on the western margin of the edifice show approximate elongation N–S, and likewise on the east of the complex a group of clustered craters shows overall elongations in N–S and NE–SW directions. The distribution of volcanic vents (Figs. 4 and 5) also shows a dominantly elliptical ring distribution on the main edifice with a marked absence of vents within the center of the caldera. Figure 4 shows that a number of vents on the main edifice (62% of total mapped using the lidar) are within ±500 m uncertainty of the proposed ring structure. Vents that are not within this structure may have been controlled by other structures (e.g., the Artu Jawe fault zone; see following), or alternatively the caldera ring fault may be more structurally complex than the proposed

ellipse. Caldera ring faults are unlikely to truly approximate an ellipse in shape; however, this is the simplest first-order model of a ring fault in the absence of other evidence concerning its structure.

The vent elongations and distributions match orientations that would be expected for a mature caldera structure feeding eruptions at the surface. We assume that feeder dikes here are either elongate in response to the local stress field set up on the caldera or are directly exploiting an existing ring fracture. The ellipse fit is ~5 km in N–S diameter and ~8 km in E–W diameter, with ellipticity (short/long axis ratio) of 0.63 and long-axis elongation of N090°E. The mapped caldera rim remnant corresponds closely to the proposed ring fracture, although it only overlaps ~8% of the entire ellipse (Figs. 4 and 5).

Evidence for Faulting

The deep well stratigraphy (Fig. 2B) reveals several major fault zones, aligned with regional tectonic trends, dissecting the Aluto volcanic complex. However, few of these structures have a clear surface expression, due to the large volumes of young volcanic and lacustrine sediment cover. On the edifice the surface is mantled by tephra and obsidian lava flows; to the north, west, and south of Aluto there are substantial lacustrine deposits (including gravels, sands, muds, and diatomite) that were deposited throughout the late Pleistocene and early Holocene (Grove and Goudie, 1971; Grove et al., 1975; Gasse and Street, 1978; Street, 1979; Gillespie et al., 1983; Le Turdu et al., 1999; Benvenuti et al., 2002).

The only major fault scarp visible on Aluto is exposed in a 500-m-long segment on the east of the caldera, the NNE–SSW Artu Jawe fault zone (Figs. 2A and 3A). Topographic profiles across the fault show a typical profile expected for a normal fault down throwing to the west (with a maximum throw of 50 m measured at the surface). The scarp is mostly covered by recent slumped clastic material, but in a more pristine deeper exposure a highly brecciated aphyric obsidian lava is visible (Fig. 3B). The poorly consolidated texture and thin (1–10 cm) subvertical banding of the deposit is very different from obsidian lavas encountered elsewhere on the complex and therefore may represent fault gouge. The near vertical dip and approximate north-south strike of the foliations (Fig. 3B) closely match the overall trend of the fault scarp.

To the north, the fault scarp is covered by an elongate dome of pumice and obsidian lava units (Figs. 5B and 7). This elongate dome is 2 km (E–W) by 4 km (north-south), ~180 m high, and is close to the trend of the Artu Jawe fault scarp. We infer that these volcanic deposits have erupted along the fault zone building up the elongate pumice dome. To the south of the Artu Jawe fault scarp the surface rupture is obscured by mantling tephra; however three-dimensional views of the fault zone (Fig. 7) show a gorge following the same trend, supporting its continuation into the volcanic pile. There is evidence of a secondary, less-pronounced break in topography ~500 m west of the main scarp (Fig. 7). The surface topography data alone are not sufficient to classify these faults separately. Owing to their proximity to the main scarp, we group these structures together as the Artu Jawe fault zone.

There are no clear fault traces exposed on the caldera floor (CF in Fig. 7), suggesting that either the material infilling the caldera is very young and/or there has been no significant recent displacement on faults within the caldera. It has been suggested (Kebede et al., 1985; ELC Electroconsult, 1986) that a fault gorge extends through the southern rim (SFG in Fig. 7). A line of fumaroles parallel to this gorge (Fig. 7B) provides qualitative evidence to support existence of this fault (see following discussion of hydrothermal features).

Three obsidian domes and nested craters were identified on the northwest of the caldera floor (Fig. 6C). The domes are of comparable size (150–400 m diameter) and are aligned along a trend of N050°E. In the field the domes appear compositionally similar and display similar weathering characteristics, suggesting that they share a common source and erupted at a similar time. These observations suggest an underlying tectonic control on the eruption of these lavas at the surface.

From remote sensing (Figs. 2A and 4) there is a clear prevalence of volcanic vents aligned NNE–SSW northwest of the edifice, but there is no evidence for large fault structures at the surface. Highstands in the lake system since 10 ka have reached maximum lake levels of 1660–1680 m above sea level (Street, 1979; Gillespie et al., 1983; Benvenuti et al., 2002, 2013), sufficient to isolate these vents. We therefore assume that these young lacustrine sediment deposits have masked any surface fault breaks.

Volcanic Alignments

In Figure 8 we compare the orientations of volcanic features and vent alignments with regional fault trends. As expected (e.g., Agostini et al., 2011), we can distinguish two distinct fault systems in the CMER: border faults and the younger internal faults (referred to herein as the Wonji faults). There is a marked difference in strike between the two groups (Figs. 8A, 8B). The Wonji faults have a NNE–SSW strike (mean value of N012°E); in contrast, the border faults have a more NE–SW orientation (mean value of N032°E).

Figure 8C shows a length-weighted rose plot for all crater rim and fissure line segments mapped on the main volcanic edifice (identified in Fig. 5). Unlike tectonic fault trends these features display preferential orientations along both N–S and E–W alignments. Crater rim and fissure line orientations are also skewed to NE–SW rather than NW–SE alignments (Fig. 8C). Figures 8D and 8E show the azimuth between volcanic vent locations (i.e., point features) on and off the main edifice of Aluto. On the main edifice the volcanic vent alignments (Fig. 8D) show equivalent results to those shown in Figure 8C; there is a pronounced NNE–SSW alignment (N010–020E° bin), secondary E–W alignment, and a general skew to NE–SW rather than NW–SE alignments. Off the main edifice (Fig. 8E) the results show that the prevailing vent alignment range is N000–020E°.

The preferential E–W orientations observed in Figure 8C arise due to the large number of elongated craters (clearly present on the southern rim of the complex; Fig. 5). Figures 8C and 8D both support the existence of E–W-oriented structures feeding surface eruptions; following the preceding discussion, it is assumed this is the surface manifestation of an underlying elliptical caldera structure. Crater and fissure line orientations (Fig. 8C) as well as vent alignments (Fig. 8D) also show N–S and NNE–SSW orientations; these are representative of aligned elongate craters on the east and west margins of the caldera ring structure (Fig. 5) but also alignments along the major tectonic fault structure (Artu Jawe fault zone). Off the main edifice (Fig. 8E) vent alignments are very close to the observed fault strike of the Wonji faults (Fig. 8A), strengthening the case that beyond the caldera tectonic fault structures are the dominant control on magma pathways.

Hydrothermal Features

Figure 4 shows the zones of hydrothermal alteration, fumaroles, and hot springs mapped using the aerial photos and supplemented by mapping reports from the Geological Survey of Ethiopia (Kebede et al., 1985). A summary of the main hydrothermal features and their links to the volcanic and tectonic structures is provided in Table 1.

The sites of hydrothermal activity are confined to the summit and flanks of Aluto, as well as the region of hot springs around the north bay of Lake Langano (Fig. 4). There is no evidence of active or fossil hydrothermal activity on the northern and eastern flanks of the Aluto edifice.

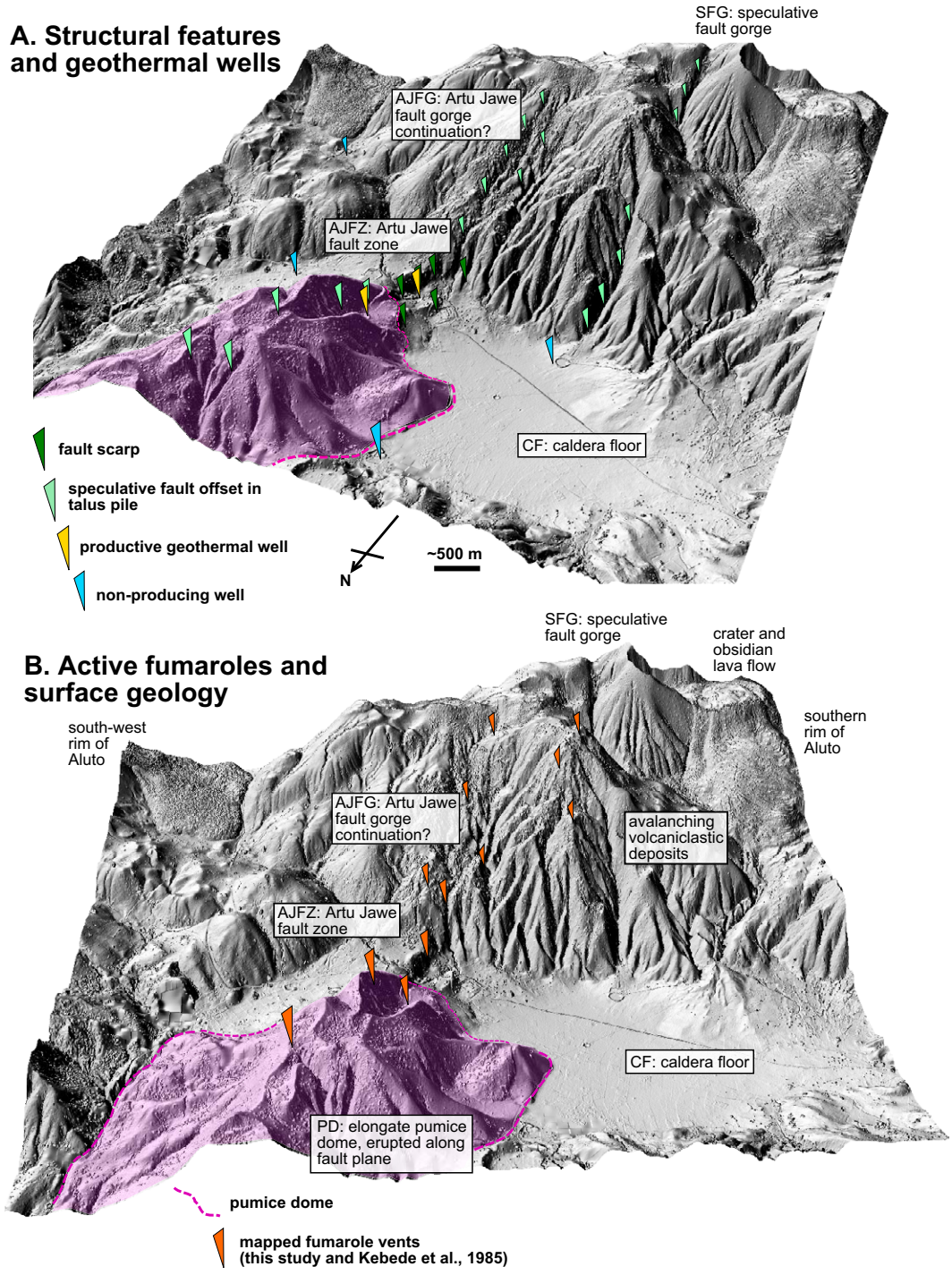

Figure 7. Three-dimensional view of the hillshade DEM covering the Artu Jawe fault zone. (A) Fault scarps and their possible continuation into the volcanic pile (indicated by deep gorges); geothermal wells are also shown (the only productive wells are located adjacent to the major fault scarp). (B) Fumaroles identified either in the field or using locations reported from field mapping by the Geological Survey of Ethiopia (Kebede et al., 1985). The pink shaded area and dashed line delimit the pumice dome (Fig. 5); the elongate nature of the dome is interpreted to reflect the underlying tectonic control.

Along the Artu Jawe fault zone (Fig. 5) fumaroles continue both north and south of the fault scarp (Figs. 5 and 7B), indicating that the fault continues beneath the young volcanic cover (Fig. 7A). Hydrothermal alteration is also found at the base of the remnant caldera rim (Fig. 4), where several zones of fumaroles are seen emanating from fractures in altered lava (Fig. 3C; Bobesea, Table 1). The lines of fumaroles (identified in Fig. 3C) follow a NW–SE trend, identical to the orientation of the caldera rim, and thus are linked to a buried ring fault.

Not all hydrothermal features on Aluto can be correlated with mapped structures. For example, on the west flank of Aluto fumaroles occur over a large area at Hulo and Auto (HL and AT in Fig. 4) and while these may link to structures and aligned volcanic vents northwest of the edifice, evidence for a tectonic control at the surface is absent (Fig. 6B). On the southern flank of Aluto, fumaroles at Kore and Gebiba (K and GB in Fig. 4) also show no clear structural association.

CO_2 Degassing

The CO_2 flux values measured on Aluto span several orders of magnitude, varying between 0.5 and 40,000 g m^{-2} d^{-1}. Background CO_2 flux measurements at locations 10–20 km away from

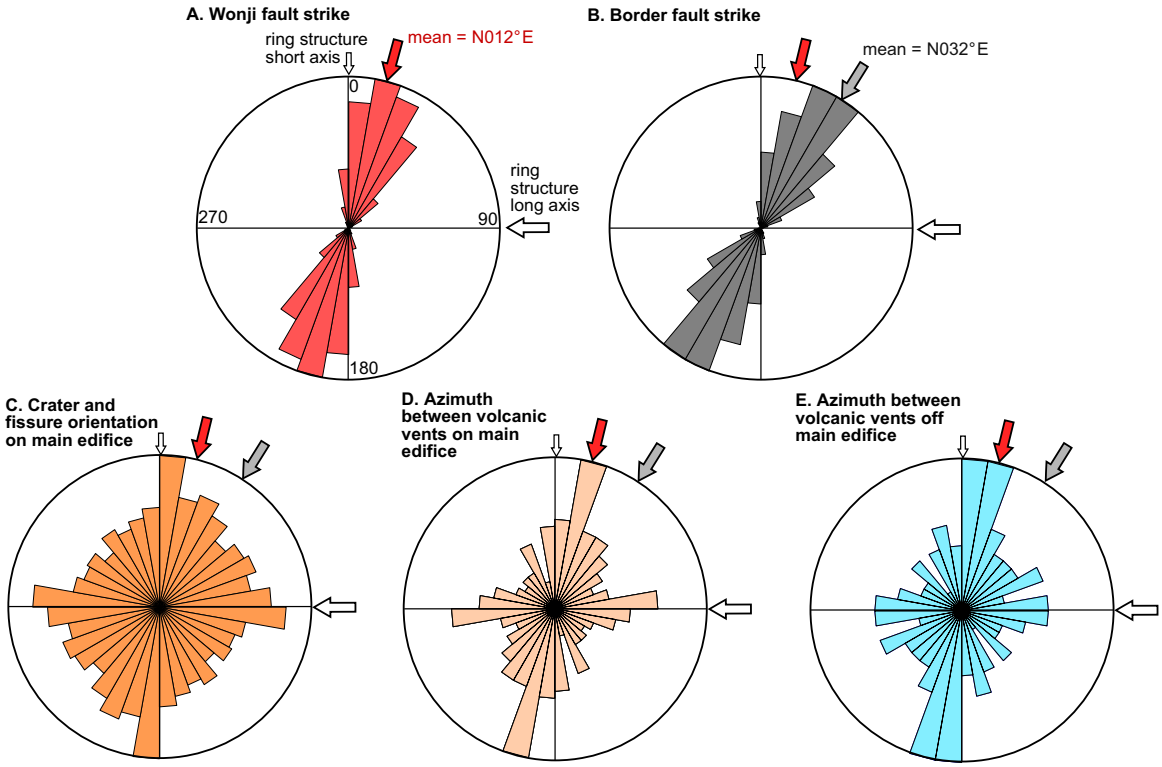

Figure 8. Rose plots comparing regional fault trends, volcanic crater rim and fissure orientation and vent alignments, shown as trends in degrees from north (i.e., 0° = north; 90° = east; 180° = south). Arrows are used to identify the long and short axis of the ring structure (white), which has an approximately E–W elongation; the mean trend of the Wonji faults (red); and the mean trend of the border faults (gray). (A, B) Regional fault strike for the Wonji and border faults of the central Main Ethiopian Rift analyzed using the Agostini et al. (2011) database (available online at http://ethiopianrift.igg.cnr.it/utilities.htm). (C) Length-weighted rose plot that analyzes the orientation of all crater rim and fissure line segments mapped using the lidar data set (shown in Fig. 5B) to identify prevailing orientations of elongate vents and fissure features. (D, E) The azimuth between neighboring volcanic vents, analyzed using the vent locations (black point features) in Figures 4 and 5. Vent azimuth is analyzed both on and off the main edifice (i.e., the area covered by the lidar; Fig. 5). The data are filtered such that only those vents separated by 0.2–2 km are analyzed. A number of different distance filter windows were explored and while the 0.2–2 km filter window is shown here, the results of similar size windowing methods between 0.1 km and 4 km tended to produce comparable results.

Aluto ranged from 0.5 g m^{-2} d^{-1} in rocky organic-poor soils to 6 g m^{-2} d^{-1} in darker organic-rich soils (i.e., vegetated areas with more abundant leaf litter). A flux of 6 g m^{-2} d^{-1} was taken as the upper limit for a purely biogenic background CO_2 flux in the study area. These fluxes are low when compared to values that characterize soils in less arid climates, 10–30 g m^{-2} d^{-1} (Mielnick and Dugas, 2000; Rey et al., 2002; Cardellini et al., 2003).

Transects Across Major Structures

The CO_2 degassing transects across the main structural features (A–A′, B–B′, C–C′; Fig. 5A) correspond with lidar-derived topography and soil CO_2 flux profiles shown in Figure 9. Profile A–A′ is along the center of the volcanic complex across the caldera floor and intersects the Artu Jawe fault zone to the east. The topography reveals the smoothly downward-curving caldera floor and the well-defined ~50 m offset across the fault zone. The CO_2 flux through the caldera floor is below or very close to the background biogenic flux value. The absence of significant degassing through the caldera floor is in line with remote sensing observations that did not indicate any clear fault offsets. Adjacent to and within 500 m of the fault scarp the CO_2 flux is significantly above the background levels. The scale in Figure 9 (A–A′) was chosen to illustrate the small variations in the low fluxes, and maximum values measured along the fault zone were >10,000 g m^{-2} d^{-1} (the full range of flux values along the fault zone is shown in Fig. 10).

Profile B–B′ transects the remnant caldera rim structure. The CO_2 flux shows greatest values (to 1850 g m^{-2} d^{-1}) at the base of the caldera rim, with lower values (2–7 g m^{-2} d^{-1}) to the southwest and on the caldera rim. The area of anomalous degassing is defined by several sets of fumaroles; CO_2 flux values are greatest on fumaroles (500–1850 g m^{-2} d^{-1}) and lower in cohesive soils between the open fractures (15–240 g m^{-2} d^{-1}; Fig. 3C).

Profile C–C′ follows the topographic high on the southern rim of the complex. The CO_2 flux values increase from low background values (<6 g m^{-2} d^{-1}) to 11 g m^{-2} d^{-1} at the peak and immediately south of the rim. Elevated CO_2 flux values coincide with the hypothesized location of the ring fault. However, the maximum values encountered at the peak were significantly lower than those found on profile B–B′, and no evident structural feature was exposed at the surface.

TABLE 1. SUMMARY OF THE MAIN HYDROTHERMAL FEATURES ON THE ALUTO VOLCANIC COMPLEX

Area	Easting (m)	Northing (m)	Maximum temperature at 5–15 cm (°C)	Maximum CO_2 flux (g m^{-2} d^{-1})	Structural association	Notes
Hulo (HL)	469800	860300	95†	ND	West Aluto fault	Large area of hydrothermal alteration with several groups of fumarole vents
Auto (AT)	470000	861300	94†	ND	West Aluto fault	Fumaroles located southeast of well LA-2 on west flank of Aluto (Fig. 2D), significant alteration of pumice to red/orange clays
Adonshe (AD)	472700	861900	85†	ND	Continuation of NE–SW fault?	Altered pumiceous ground through which fumaroles are issued
Humo (HM)	474000	860900	77†	ND	Unknown	Low-temperature fumarole outlets extending along gorge
Worbota (WB)	474300	863200	85*	2300	NE–SW fault or ring fault?	Steaming ground found in small crater and patches of orange/brown altered ground within 1 km
North Bay (NB)	475000	852300	67†	ND	Outflow along water table	Several springs located along the northern shore of Lake Langano
Oitu Artu (OA)	475100	856200	94†	ND	Continuation of Artu Jawe fault zone?	Fumaroles exposed in N–S oriented gorge, fumaroles emanate from rhyolite lava units at base of gorge, surrounding pumices is altered to yellow/red clay, fumaroles have H_2S smell
Edo Laki (EL)	475100	850400	95†	ND	Unknown	Hot springs and mud pools along the shore of the island
Artu Jawe (AJ)	476500	860200	95*	10,000–40,000	Artu Jawe fault zone	Large groups of fumaroles located east of power plant, steam has H_2S smell, alteration of rhyolite and pumice surface lithologies
Finkilo (FK)	477100	859200	85†	ND	Artu Jawe fault zone	Groups of fumaroles emanating from rhyolitic lava units in N–S-oriented gorge, H_2S smell, alteration of surface rocks to red-brown clays
Kore (K)	477800	857700	95†	ND	Hidden NNE–SSW-trending fault or lateral outflow from Artu Jawe fault zone?	Fumaroles aligned in north-south running gorge, issued through rhyolite lava
Gebiba (GB)	478500	855900	95*	5400	Hidden NNE–SSW-trending fault or lateral outflow from Artu Jawe fault zone?	Fumaroles at base of gorge oriented NNE, H_2S smell, alteration of pumice to red/gray clays
Bobesea (BOB)	480100	861000	93*	1850	Ring fault	Fumarole vents extend in several NW–SE-rending ridges (parallel to remnant caldera rim), large area of hydrothermal alteration where pumices are altered to red/gray clays

Note: Abbreviations of areas are keyed to locations given in Figure 4 (see text). ND—no data.
*Ground temperature measurements made in the field with thermocouple during this study.
†Ground temperature measurements made in the field with thermocouple by Kebede et al. (1985).

Artu Jawe Fault Zone

On profile A–A′ (Fig. 9), there are considerable CO_2 flux variations encountered in the fault zone. To better constrain these variations along the fault, we undertook a high-resolution (30 m) sampling survey. Figure 10 provides topography, surface geology, and soil CO_2 flux results for the survey area (outlined in Fig. 5B). The shaded relief DEM (Fig. 10A) identifies the main ~50-m-high fault scarp (Fig. 3A) and its projected continuation north, where it is obscured by pumice dome deposits (identified in Figs. 5B and 7). To the west of the main fault scarp there are a number of smaller breaks in topography (10–20 m high) (white dashed lines in Fig. 10A).

Figure 10B shows the surface geology map. The area is largely covered in young tephra (pumice fall and pyroclastic deposits) sourced either from the pumice dome to the north of the study area (Figs. 5B and 7) or from eruptive vents on the southern rim of the caldera complex. At the base of these slopes, tephras were reworked by fluvial processes and are represented by fine-grained alluvium and gravel deposits. A porphyritic obsidian flow is located on the west of the grid. The obsidian flow is likely sourced from a vent at the base of the cliff; however, recent avalanching of the volcaniclastic deposits in the cliff has obscured the exact position of the vent.

The soil CO_2 flux map (Fig. 10C) shows that the flux varies by several orders of magnitude across the survey area, while a log probability plot (Fig. 10D) shows a bimodal distribution confirming the existence of two distinct CO_2 sources (i.e., background biogenic and volcanic hydrothermal; Chiodini et al., 1998) that contribute to the degassing. The highest CO_2 flux values are found close to fumarole vents, suggesting that in those areas CO_2 travels mostly with hydrothermal steam. From the mean of the simulations the total diffuse CO_2 emission for the 800,000 m^2 grid (Fig. 10C) is calculated as 62 ± 12 t d^{-1}.

Transect lines shown in Figure 10C link to Figure 11, which show the topography and flux measurements along the profile line. On profile W–W′, peak flux values occur at the base of the main cliff, associated with a fault plane. Profiles X–X′ and Y–Y′ (Fig. 11) cross the ridge of pyroclastic deposits east of the fault and also show a relationship between CO_2 flux and topography, with peak values in CO_2 flux close to but slightly displaced from the absolute topographic high. Profile Z–Z′ crosses several lithologies on the west of the grid; CO_2 flux values are on average lower on the obsidian lava flow deposits compared to the tephra deposits to the north and south.

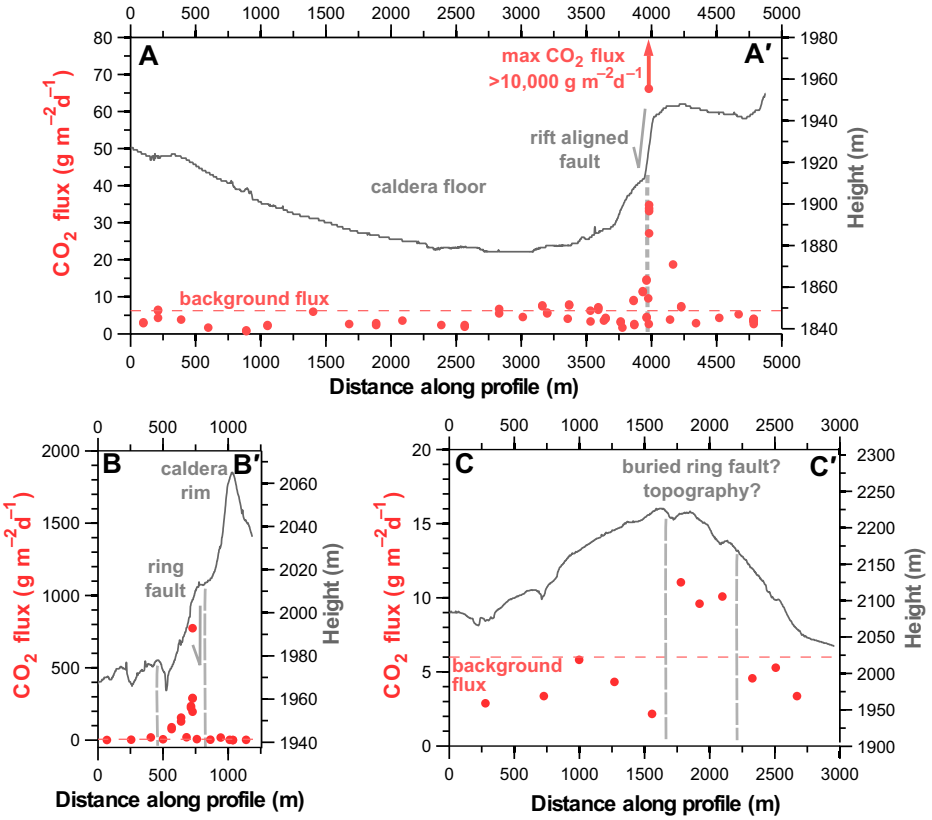

Figure 9. CO_2 degassing transects across the major structural features (Fig. 5), including the Artu Jawe fault zone, A–A′; the remnant caldera rim, B–B′, and the southern rim of the complex, C–C′. The red points give the observed CO_2 flux (left axis), and the gray line gives the topography (right axis). Note differences in vertical scales between plots.

DISCUSSION

Tectonic Features Dissecting the Volcano

The results of this study, combined with prior mapping and geothermal well data (Dakin and Gibson, 1971; Di Paola, 1972; Kebede et al., 1985; Gebregzabher, 1986; Valori et al., 1992; Gizaw, 1993; Gianelli and Teklemariam, 1993), show that the Aluto volcanic complex has been dissected by normal faults related to the regional extensional tectonics, which have in turn influenced the distribution of volcanic products. The aligned vent trains that cross Aluto reflect magma pathways controlled by faults. Young vents and craters on and off the main edifice show a prevailing alignment to the regional NNE–SSW strike of the Wonji faults (Figs. 4 and 8), although there is field evidence that minor NE–SW-oriented structures may also exist (Fig. 6C).

Physical evidence for the link between faults and volcanic activity is particularly clear along the Artu Jawe fault zone, where magma has erupted along the fault, building an elongate pumice dome (Figs. 5B and 7). The Artu Jawe fault zone remains a high permeability pathway through which steam (Fig. 4) and CO_2 (Fig. 10C) ascend to the surface, as evidenced by the zones of fumarolic alteration and peaks in CO_2 flux along the fault structure (A–A′; Figs. 7 and 9). Our work shows that hydrothermal mapping (Figs. 4 and 7) and CO_2 soil-gas surveys (Fig. 10C) can be used to identify high permeability zones, revealing the locations of hidden fault structures when multiple observational data sets are considered together (e.g., Figs. 7 and 10).

Understanding the initiation and growth of these faults is critical to address the development of the Aluto volcanic complex. At present the best evidence for major fault zones on Aluto, and the only constraints on their development, are provided by the deep wells. Of particular significance is a Pleistocene lacustrine horizon that can be correlated between wells (Fig. 2B; Gianelli and Teklemariam, 1993; Gizaw, 1993) and shows a stepped west to east thinning suggestive of faulting. This unit is beneath the volcanic products of Aluto (Fig. 2B), implying that significant faulting preceded surface silicic volcanism, and hence these preexisting faults may have controlled magmatic processes throughout the growth of Aluto. Investigations of the Soddo region in the southern MER by Corti et al. (2013b) found a similar relationship, with both basaltic and rhyolitic volcanic centers following closely preexisting border faults.

Aluto Caldera

A number of previous studies have suggested that Aluto has undergone a caldera-forming event (Dakin and Gibson, 1971; Le Turdu et al., 1999), and our observations help to confirm this. Taking together the presence of a remnant caldera rim (Figs. 2A, 4, and 5), the occurrence of eruptive vents on an elliptical (ring) structure (Figs. 4 and 5) and the correspondence of this to zones of hydrothermal alteration (Fig. 4) and local peaks in CO_2 degassing (B–B′, C–C′, Fig. 9), we propose that an underlying ring fracture system that matches the mapped caldera rim remnant can explain these observations.

A major challenge in defining this structure is that the exposure of the remnant caldera rim is limited to the northeast of the complex (only covering ~8% of the ellipse; Fig. 4). We assume that the rest of the structure has been covered by post-caldera volcanic deposits or eroded. This is typical of peralkaline volcanic edifices that undergo repeated phases of caldera collapse and caldera-filling volcanism (Cole et al., 2005) that overspill the caldera rim and mask its surface expression (Mahood, 1984). The size (~8 km × ~5 km) and shape of the proposed Aluto ring structure (Figs. 4 and 5B) are similar to other peralkaline complexes in the MER (Cole, 1969; Mohr et al., 1980; Acocella et al., 2003; Rampey et al., 2010), and within the upper range of other peralkaline calderas worldwide (Mahood, 1984; Cole et al., 2005). The caldera wall on Aluto (>50–60 m in height) is comparable to other peralkaline calderas where subsidence is a few hundred meters (Mahood, 1984).

The elliptical caldera form is typical of continental rift volcanoes worldwide (e.g., Wilson et al., 1984; Acocella et al., 2003; Bosworth et al., 2003; Casey et al., 2006; Geyer and Marti, 2008). Elliptical calderas may be produced by a number of different mechanisms (Holohan et al., 2005), including (1) collapse of an elliptical magma reservoir; (2) nesting, where multiple collapse structures overlap and give rise to an elongate geometry; (3) shallow crustal processes, where asymmetric collapse, or distortion of caldera faults leads to an asymmetric caldera above a circular magma chamber; and (4) post-caldera modification, where a circular caldera is distorted by erosion or regional deformation. Ultimately, the infilling of the Aluto caldera has

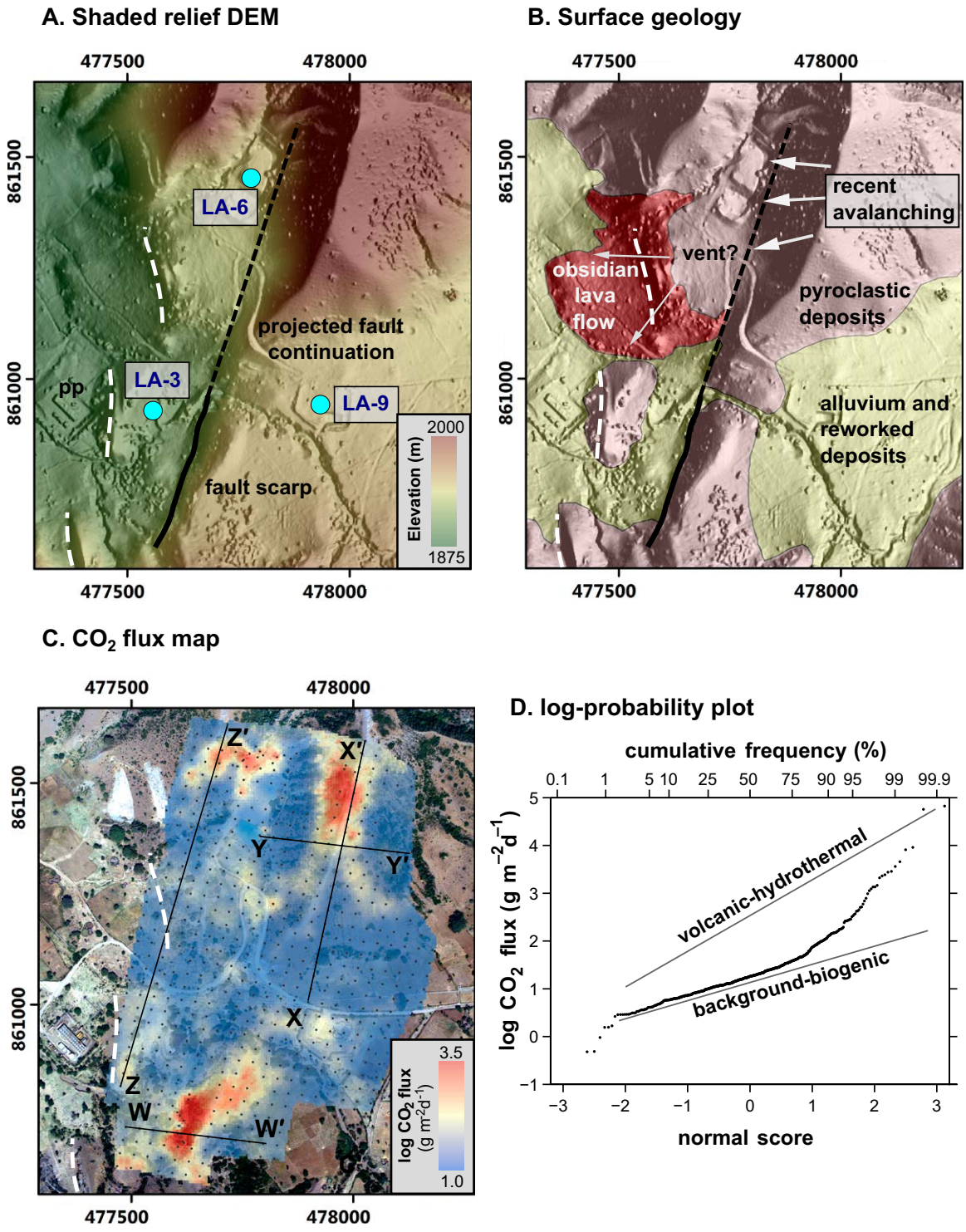

Figure 10. Focused study of degassing along the Artu Jawe fault zone. (A) Shaded relief digital elevation model (DEM) showing the Artu Jawe fault scarp (black) and its projected continuation north (dashed). Less-pronounced breaks in topography (10–20 m high) west of the main fault scarp are marked by white dashed lines (these are also visible in in Fig. 7). Blue points identify the location of the productive geothermal wells (LA-3 and LA-6), as well as the site of the new well (LA-9); pp—the Aluto-Langano geothermal power plant. (B) Surface geology map constructed from the observations of the exposure noted at each grid locality and further discriminated using the aerial photos. Surface geology consists of pyroclastic deposits (pink), alluvium (yellow), and obsidian lava (red). (C) CO_2 flux map derived using the sequential Gaussian simulation (sGs) approach. Gray points represent a discrete flux measurement. W–W′, X–X′, Y–Y′, and Z–Z′ are transects in Figure 11. (D) Probability plot of soil CO_2 flux values from the survey grid identifying background and volcanic-hydrothermal populations in the distribution (for detailed explanation of application of probability plots to CO_2 flux data sets, see Chiodini et al., 1998).

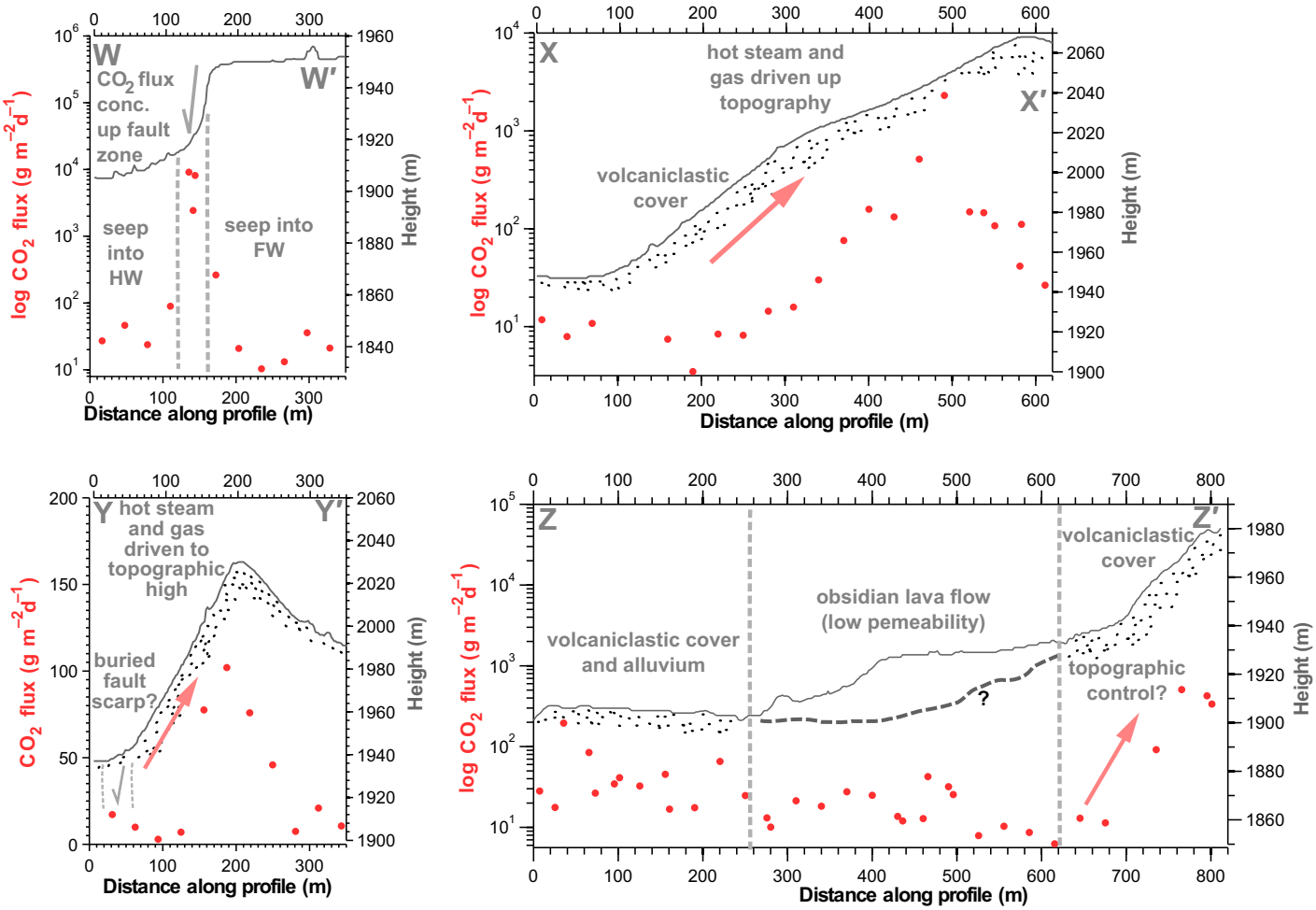

Figure 11. CO_2 degassing transects across the Artu Jawe fault zone that correspond to the transect lines W–W′, X–X′, Y–Y′, and Z–Z′ in Fig. 10C. HW—hanging wall, FW—footwall, conc.—concentrated. The red points give the observed CO_2 flux (left axis), and the gray line gives the topography (right axis). Black stipples indicate poorly consolidated volcaniclastic deposits or alluvial cover. Note differences in vertical scales between plots.

left little information concerning the original collapse structure and the nature of the collapse event. In particular, it is unclear whether the caldera collapse involved one or multiple events, to create a nested structure (as is typical for peralkaline volcanic complexes; Mahood and Hildreth, 1983; Mahood, 1984; Rampey et al., 2010). It is also not possible to infer whether collapse was asymmetric or whether subsidence was accommodated by existing tectonic faults. Assuming that collapse took place at 155 ka, the only age constraint for the major ignimbrite deposits of Aluto (ELC Electroconsult, 1986), and assuming current extension rates of 5 mm yr^{-1} (Bendick et al., 2006; Stamps et al., 2008), then this would generate <1 km of extension since caldera formation (i.e., not sufficient to explain all of the E–W elongation).

The elliptical calderas of the East African Rift system are frequently linked to the collapse of elongate magma chambers (e.g., Bosworth et al., 2003; Acocella et al., 2003). The genesis of elongate magma chambers in a continental rift currently revolves around two distinct models, one related to the regional extensional stress field causing differential spalling of the walls of the magma reservoir (Bosworth et al., 2003), and the other related to preexisting structural weaknesses, such as pre-rift faults, facilitating preferential magma chamber development (Acocella et al., 2003). To explain caldera elongation using the preexisting structures model requires a detailed understanding of the evolution and orientation of regional fault patterns. For example, Acocella et al. (2003) identified a number of E–W-oriented pre-rift tectonic structures on the flanks of the MER and invoked these to explain elongate calderas at Fentale, Kone, and Gedemsa. We investigated fault maps of the MER presented by Acocella et al. (2003), Abebe et al. (2007), and Agostini et al. (2011), as well as our own satellite imagery and could not highlight any clear E–W structures on the rift plateau adjacent to Aluto. On the other hand, however, the E–W elongation of the Aluto caldera is almost orthogonal to the active Wonji faults of the central MER (Fig. 8A) and parallel to the Nubia-Somalia displacement vector (~N100°E; Bendick et al., 2006; Keir et al., 2006; Pizzi et al., 2006; Stamps et al., 2008). This observation is consistent with the idea that the regional stress field played a role in magma reservoir development at Aluto (cf. Bosworth et al., 2003).

Compared to neighboring MER volcanoes, Aluto has undergone considerable post-caldera volcanism. Shala (Mohr et al., 1980), Gedemsa (Peccerillo et al., 2003), and Kone (Cole, 1969; Rampey et al., 2010) volcanoes have all undergone caldera-forming eruptions; however, post-caldera activity has been modest, building up small domes of pumice and obsidian (within the caldera and adjacent to the caldera ring fault).

At Corbetti, two silicic cones (Chabbi and Urji) have built up within the caldera (Mohr, 1966; Di Paola, 1971). Chabbi, the larger and more voluminous of these, has built up on the east of the caldera floor and now completely covers the caldera wall on the eastern side of the complex (Di Paola, 1971). This may provide a possible analogue to Aluto, which has undergone widely distributed post-caldera volcanism along the ring fracture, and thus only a small segment of the caldera wall is retained (Fig. 4).

Controls on CO_2 Degassing and the Hydrothermal System

Volcanic CO_2 Degassing

At the edifice scale, both regional tectonic faults (such as the Artu Jawe fault zone; A–A′, Fig. 9) and the volcanic ring fracture (B–B′, Fig. 9) have a strong control on diffuse CO_2 emissions. The escarpment of the Artu Jawe fault zone (W–W′ in Fig. 11) shows that CO_2 gas is concentrated along the fault plane and that flux values remain high over a ~50-m-wide high permeability crushed zone across the fault. Across the southern rim of the complex we find elevated CO_2 fluxes spread over a ~500-m-wide zone (C–C′, Fig. 9), where we infer that a ring fault is deeply buried beneath a thick pile of volcanic deposits. Without deep penetrating structures connecting reservoir to surface, significant soil-flux degassing peaks (such as A–A′, B–B′, Fig. 9) are unlikely to be observed.

Substantial variations in the spatial pattern of CO_2 degassing are evident both parallel and transverse to the major structures when observed at scales <100 m (Fig. 10C). These are linked to permeability variations in the near surface (Schöpa et al., 2011; Pantaleo and Walter, 2013) possibly caused by changes in lithology or changes in the topography-induced stress field (that focuses the permeable pathways toward the morphological crests). There is a correlation between local topography and degassing flux (Fig. 11, X–X′, Y–Y′) in the pumice dome (Fig. 10). Our interpretation is that the pumice dome deposits have buried the Artu Jawe fault scarp, and thus steam and gas rising up along the fault plane enter the base of the dome and become focused toward the morphological ridge crest. A similar morphological control has been observed at Vesuvius (Italy), where CO_2 anomalies are concentrated in the inner slopes of the crater rim (Frondini et al., 2004). The key difference on Aluto is that CO_2 gas and steam are fed into the base of the volcanic pile from a tectonic fault rather than a volcanic conduit.

Several (e.g., Peltier et al., 2012; Pantaleo and Walter, 2013) have studied the influence of surface lithology and soil texture on permeability, and our data set permits a qualitative assessment for Aluto. Profile Z–Z′ (Fig. 11) crosses several contrasting lithologies west of the Artu Jawe fault scarp; CO_2 fluxes are on average lower on the obsidian lava flow deposits compared to pumiceous deposits north and south. This could be evidence that the lower permeability obsidian lava flow restricts or deflects gas flux relative to the more permeable, poorly consolidated clastic deposits.

The total CO_2 flux value of 62 t d^{-1} calculated along the 0.8 km^2 section of the Artu Jawe fault zone represents both the volcanic-hydrothermal and biogenic CO_2 flux. Assuming that a mean biogenic flux of 6 g m^{-2} d^{-1} is constant over the survey area, subtracting this contribution from the total CO_2 release would give a total volcanic-hydrothermal CO_2 emission of 57 t d^{-1}. This is comparable to other sites of volcanic CO_2 degassing worldwide (Table 2), and when standardized to a CO_2 flux per area (71 t d^{-1} km^{-2}), it is similar to geothermal sites in other rift zones, such as the Reykjanes geothermal area (Iceland; Fridriksson et al., 2006), and Taupo volcanic zone (New Zealand; Werner and Cardellini, 2006). Given that the total area of hydrothermal alteration and degassing features on Aluto (Fig. 4) is 5–10 times larger than the area covered by the CO_2 flux survey (Fig. 10C), we expect total CO_2 emission from Aluto to be 250–500 t d^{-1}. This magnitude of diffuse CO_2 release is comparable to a number of other volcanoes that have either undergone Holocene eruptions and/or show signs of unrest, e.g., Pululahua caldera (Ecuador), Vesuvius, Teide (Canary Islands), and Rotorua (New Zealand) (see Table 2). The estimated CO_2 flux for Aluto is also comparable to mean volcanic plume CO_2 fluxes measured at active volcanoes such as Merapi (Indonesia), Vulcano (Italy), Sierra Negra (Ecuador), and Villarrica (Chile) (see Burton et al., 2013, and

TABLE 2. COMPILATION OF DIFFUSE CO_2 EMISSIONS FROM SELECTED VOLCANIC DEGASSING AREAS OF THE WORLD

Study area	CO_2 flux (t d^{-1})	Area (km^2)	CO_2 flux density (t km^{-2} d^{-1})	Reference
Cuicocha caldera, Ecuador	106	13.3	8	Padrón et al. (2008)
Pululahua caldera, Ecuador	270	27.6	10	Padrón et al. (2008)
Pantelleria island, Italy	989	84	12	Favara et al. (2001)
Oldoinyo Lengai, Tanzania*	100	3.14	32	Koepenick et al. (1996)
Satsuma-Iwojma volcano, Japan	80	2.5	32	Shimoike et al. (2002)
Iwojima volcano, Japan	760	22	35	Notsu et al. (2005)
Vesuvius, Italy	193.8	5.5	35	Frondini et al. (2004)
Mount Epomeo, Italy (western flank)	32.6	0.86	38	Chiodini et al. (2004)
Vulcano island, Italy (western and southern slopes)	75	1.9	39	Chiodini et al. (1998)
Nisyros caldera, Greece	84	2	42	Cardellini et al. (2003)
Yanbajain geothermal field, China	138	3.2	43	Chiodini et al. (1998)
Reykjanes geothermal area, Iceland	13.5	0.22	61	Fridriksson et al. (2006)
Rotorua geothermal system, Taupo Volcanic Zone, New Zealand	620	8.9	70	Werner and Cardellini (2006)
Aluto, Ethiopia (Artu Jawe fault zone)	57	0.8	71	This study
Miyakejima volcano, Japan (summit)	100–150	0.6	167	Hernández et al. (2001)
Furnas volcano, São Miguel Island, Azores	968	5.2	186	Viveiros et al. (2010)
Hakkoda volcanic area, Japan (localized flank area)	127	0.58	219	Hernández Perez et al. (2003)
Methana volcanic system, Greece	2.59	0.01	259	D'Alessandro et al. (2008)
Hot Spring Basin, Yellowstone	60	0.16	387	Werner et al. (2008)
Mud volcano, Yellowstone	1730	3.5	494	Werner et al. (2000)
Liu-Huang-Ku hydrothermal area, Taiwan (phreatic crater)	22.4	0.03	659	Lan et al. (2007)
Teide volcano, Spain (summit area)	380	0.53	717	Hernández et al. (1998)
Mammoth Mountain, Horseshoe Lake (flank area)	104.3	0.13	802	Cardellini et al. (2003)
Nea Kameni, Santorini, Greece (summit area)†	21–38	0.02	1050–1900	Parks et al. (2013)
Solfatara volcano, Italy	1500	1	1500	Chiodini et al. (2001)
Cerro Negro volcano, Nicaragua	2800	0.58	4828	Salazar et al. (2001)

Note: Compilation is after Viveiros et al. (2010) and Burton et al. (2013).
*Measurements assume CO_2 emission restricted to the summit and flank area with diameter of 2 km.
†Measurements made across a period of volcanic unrest (Parks et al., 2013).

references therein). Degassing measurements at continental rift zone volcanoes are sparse, especially soil CO_2 surveys (Koepenick et al., 1996), and no such surveys have been undertaken at the silicic caldera-forming volcanoes of the East African Rift system (such as Aluto) that constitute an important class of rift volcanism. This highlights the significance of the CO_2 degassing surveys presented here, and future surveys of the East African Rift system volcanoes to constrain carbon and other volatile element fluxes are to be encouraged.

Hydrothermal System

Our observations of hydrothermal features on Aluto (Fig. 4) confirm that the mapped faults provide key pathways for the upflow of geothermal fluids. A number of the fumarole sites do not align with these structures; this suggests that they are controlled by otherwise hidden fractures or are influenced by other subtle permeability parameters (e.g., topography or lithological controls; Schöpa et al., 2011). Hot springs located along the shore of Lake Langano (Fig. 4) likely mark the outflow of the hydrothermal fluids at the water table. This is supported by shallow temperature data from well LA-1 on the south flank of Aluto (Gizaw, 1993), and evidence of silicified beach sediments 100 m north of present springs indicating that these springs follow lake levels and therefore are tied to the level of aquifer (Kebede et al., 1985). Despite the close proximity of Aluto to the lakes of Ziway, Langano, and Abijta (Fig. 1), oxygen isotope measurements of geothermal fluids conducted by Darling et al. (1996) show that >90% of the water in the Aluto geothermal system is derived from rainfall from the rift shoulders with a minimal component (<10%) derived from lake waters. The geothermal fluids are of alkali-chloride-bicarbonate type, and display geochemical evidence for interaction with rhyolitic volcanic products (Gianelli and Teklemariam, 1993). This observation along with deep well temperature and stratigraphy data (Gizaw, 1993; Gianelli and Teklemariam, 1993; Teklemariam et al., 1996) support the Tertiary ignimbrite deposit (Fig. 2B) being the reservoir for the geothermal field.

Conceptual Model

A conceptual model is provided in Figure 12 that captures both the evolution of the complex and the role the major structures have on controlling fluid pathways. While the timing of the initiation of the tectonic fault structures remains poorly constrained, the existing evidence from deep well lacustrine sequences (Fig. 2B; Gianelli and Teklemariam, 1993; Gizaw, 1993) suggests that prior to surface volcanism fault structures were active, leading to fault-bounded blocks (Fig. 12A). The Aluto volcanic complex developed before 155 ka (ELC Electroconsult, 1986) building a substantial silicic volcanic shield on the faulted surface. The complex then underwent a large caldera-forming eruption, developing a caldera rim structure (Figs. 4 and 5) and ring fault (Fig. 12B). Following collapse, significant post-caldera volcanism took place at Aluto (Fig. 12C), and the caldera structure and regional tectonic faults that dissect the volcano provided magma pathways to the surface, resulting in the development of aligned volcanic domes in NNE–SSW orientations (close to the strike of the Wonji faults; Fig. 8) and to a prevalence of recent volcanic activity around the rim of the volcano (Fig. 5B). A geothermal field has developed on Aluto (Fig.12C). Fluids are capped in an ignimbrite reservoir beneath the complex (Ginanelli and Teklemariam, 1993), and the Artu Jawe fault zone provides the major pathway for hydrothermal fluids and gases to ascend to the surface (Fig. 9, A–A′; Fig. 10C).

InSAR evidence (Biggs et al., 2011) has shown that Aluto has undergone a number of ground deformation events over the past decade. No evidence exists to suggest that this activity correlates with any changes in industrial geothermal power development on the complex, and so at present we assume that deformation is of natural magmatic or hydrothermal origin. Comparing the InSAR deformation pattern (identified by Biggs et al., 2011) to our structural interpretation, we note that (1) deformation shows an E–W elongation, (2) the deformation is approximately centered on the caldera structure center, and (3) deformation extends beyond the proposed ring fault and mapped caldera rim remnant (Figs. 4 and 5), and does not show elongation along the mapped tectonic fault structures. While the magmatic and/or hydrothermal processes driving ground deformation events on Aluto remain uncertain, an important conclusion from this study is that the structures do not appear to influence these deformation events. For example, tectonically aligned faults on Aluto do not play a role in storing fluids as has been shown at other volcanic complexes (e.g., Yellowstone, USA, where elongate deformation patterns align with mapped faults; Vasco et al., 2007). In addition, the ring structure does not constrain the area over which deformation occurs. If deformation is of hydrothermal origin this may be explained by fluid expansion in a reservoir unit that extends beyond the confines of a ring structure (as shown in Fig. 2B). Alternatively, if the deformation is magmatic, it suggests that the source may be a deep intrusion unaffected by these structures. We conclude that the mapped faults simply act as pathways facilitating shallow fluid release.

The results of this study have relevance to understanding the geothermal resources and volcanic hazards at active rift volcanoes. Regarding the geothermal field, it is clear that the Aluto complex is heavily fractured by both tectonic and volcanic structures. Of the eight exploration wells initially drilled on Aluto, only two, those on the Artu Jawe fault zone, continue to be productive. This underscores the importance of undertaking detailed geophysical surveys and structural mapping to constrain hydrothermal flow along the major structures prior to drilling. For similar structurally complex rift volcanoes that are also targets of future geothermal exploration (e.g., Corbetti, Fentale, and Dofen in the MER), it is critical to understand the key structures and their impact on subsurface fluid flow in order to maximize productivity of the field. Although these structures introduce significant complexities, fractured geothermal fields may also present new opportunities for exploitation; for example, Curewitz and Karson (1997) showed that the intersection of faults may provide efficient conduits to concentrate hydrothermal fluids in upward flow. On Aluto the intersection between the ring fault and Artu Jawe fault zone might therefore provide a suitable target for future geothermal exploration.

While the size and frequency of past eruptive activity on Aluto is poorly constrained, evidence from InSAR (Biggs et al., 2011) suggests that the complex is restless. A major result of this study is that a significant amount of recent volcanism on Aluto exploits preexisting structures. Recent volcanism at other MER complexes such as Kone (Rampey et al., 2010) and Corbetti (Mohr, 1966; Di Paola, 1971), as well as other silicic volcanic centers in the southern MER (Corti et al., 2013b), also appear to exploit existing fault structures. Future volcanic eruptions at Aluto and elsewhere in the MER are therefore likely to be facilitated by existing structures, and therefore detailed structural maps will provide an invaluable tool to assess future volcanic hazards along with conventional geological mapping and geochronology.

CONCLUSIONS AND FUTURE OPPORTUNITIES

A combination of high-resolution airborne remote sensing, field mapping, and soil CO_2 degassing surveys provides new insights into how preexisting volcanic and tectonic structures facilitate active volcanic processes in the Main Ethiopian Rift. The main outcomes of the study were as follows:

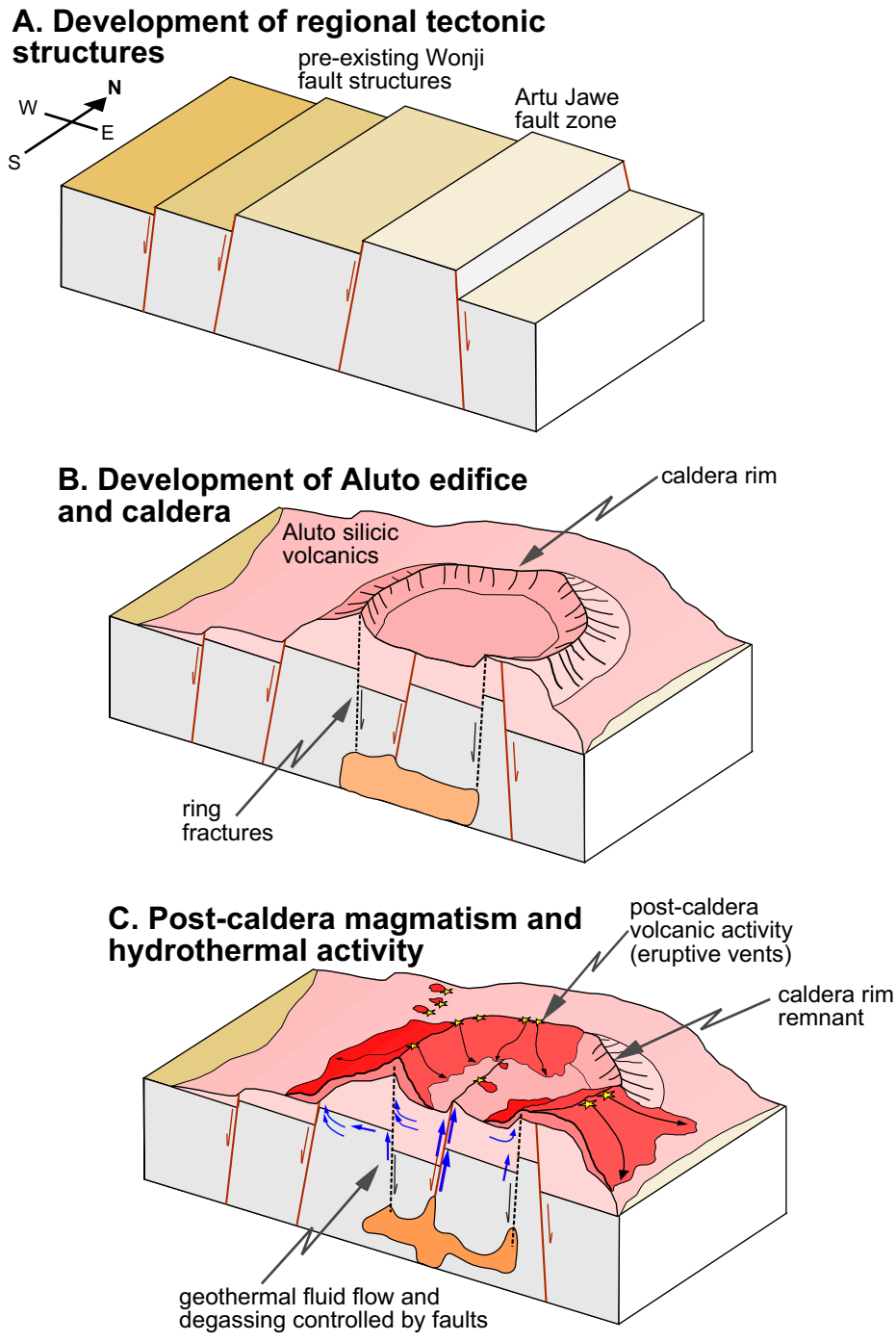

Figure 12. Conceptual model summarizing the evolution of the major structures on Aluto and their controls on surface volcanism, geothermal fluids, and degassing. (A) Regional tectonic structures aligned with the Wonji faults develop prior to surface volcanism, creating fault-bounded blocks over which abrupt lateral thickness variations in the deep well lacustrine sediments occur (Fig. 2B). (B) Surface volcanism at Aluto builds a silicic shield, which then undergoes caldera collapse. The dynamics of caldera formation remain unclear, because most of the structure has either been removed by erosion or buried by subsequent volcanic deposits. (C) Post-caldera volcanic eruptions, as well as ongoing geothermal activity and degassing processes, exploit the existing volcanic and tectonic fault network. While various fault structures provide high permeability zones for fluid flow (Fig. 9, B–B′), the Artu Jawe fault zone appears to represent the main pathway connecting the hydrothermal reservoir to the surface (Teklemariam et al., 1996).

1. Digital mapping of Aluto volcano reveals evidence for various structures on the complex. The two major structures are the Artu Jawe fault, a NNE–SSW tectonically aligned ~50-m-high fault scarp, and a 2.5-km-long caldera rim remnant that has been deeply eroded and otherwise obscured by the young post-caldera volcanic products.

2. These structures provide high permeability zones that have facilitated magma ascent and recent volcanism on Aluto, leading to vent alignments in an overall NNE–SSW orientation as well as a prevalence of vents on elliptical ring distribution pattern. These structures have facilitated past volcanic eruptions and remain open, controlling geothermal upwelling and volcanic degassing.

3. CO_2 degassing surveys conducted along the major fault zone reveal that while these structures control the ascent of gas from the deep reservoir near-surface permeability complexities, linked to lithological variations and changes in the volcanic morphology, play an important role in determining the final surface expression of degassing.

4. Overall these different observations of how lava, steam, and gas reach the surface are complementary and when integrated provide a strong case for the overarching structural controls on volcanic fluid pathways.

The new model for the structural development and volcanic edifice growth at Aluto opens up a number of avenues for future work. A major challenge is to determine how geothermal and magmatic fluids are distributed and stored in the subsurface of Aluto and how they ascend along the mapped fault zones. Further geochemical-geophysical measurements of volcanic gases (e.g., CO_2, Rn, and Th) as well as electrical resistivity and self-potential across fault planes (e.g., Giammanco et al., 2009; Siniscalchi et al., 2010) may provide vital insights into fluid circulation and the connections to the deeper reservoirs. The conceptual model (Fig. 12) lacks a detailed time frame for the initiation of faulting, volcanic edifice development, and caldera formation. Further work from both surface geology and deep wells will be needed to build a detailed chronostratigraphy, and link caldera formation with the eruptive deposits (e.g., Rampey et al., 2014). Elliptical calderas appear to be a ubiquitous feature of the MER and continental rift systems in general (Acocella et al., 2003; Bosworth et al., 2003; Geyer and Marti, 2008), and whether these elongations are related to regional stress or preexisting structures remains uncertain. Future studies should focus on generating high-spatial-resolution maps of off-rift tectonic structures and should be complemented by detailed field work to constrain the stress

field orientations during the development of the Aluto magma reservoir. Our study indicates that the magmatic and geothermal systems hosted by the MER volcanoes offer significant scope for future degassing investigations to more fully constrain the deep carbon and volatile emissions from these continental rift volcanoes to the atmosphere (Burton et al., 2013).

ACKNOWLEDGMENTS

Airborne data were collected on Natural Environment Research Council (NERC) Airborne Research and Survey Facility (ARSF) flight ET12-17-321, and initial processing was carried out by NERC ARSF Data Analysis Node (DAN). The research materials supporting this publication can be accessed from http://dx.doi.org/10.6084/m9.figshare.1261646. Hutchison, Pyle, Mather, and Biggs are supported by and contribute to the NERC Centre for the Observation and Modelling of Earthquakes, Volcanoes and Tectonics (COMET). Hutchison was funded by NERC studentship NE/J5000045/1. Additional funding for field work was generously provided by University College (University of Oxford), the Geological Remote Sensing Group, the Edinburgh Geological Society, and the Leverhulme Trust. Field assistance was provided by Elias Lewi, Tulu Bedada, Amde Zafu, Fekadu Aduna, Elspeth Robertson, Michael Hutchinson, and Girma Andarge. We also acknowledge Marie Edmonds (University of Cambridge) for loan of the LICOR LI-8100 instrument, the Geological Survey of Ethiopia for providing access to archived data and drilling reports, and the Ethiopian Electric Power Company for logistical support throughout the field campaign. We also thank J. Ruch and M. Neri for their constructive comments, which greatly improved the original manuscript.

REFERENCES CITED

Abebe, B., Acocella, V., Korme, T., and Ayalew, D., 2007, Quaternary faulting and volcanism in the Main Ethiopian Rift: Journal of African Earth Sciences, v. 48, p. 115–124, doi:10.1016/j.jafrearsci.2006.10.005.

Acocella, V., Korme, T., Salvini, F., and Funiciello, R., 2003, Elliptic calderas in the Ethiopian Rift: control of pre-existing structures: Journal of Volcanology and Geothermal Research, v. 119, p. 189–203, doi:10.1016/S0377-0273(02)00342-6.

Agostini, A., Bonini, M., Corti, G., Sani, F., and Mazzarini, F., 2011, Fault architecture in the Main Ethiopian Rift and comparison with experimental models: Implications for rift evolution and Nubia-Somalia kinematics: Earth and Planetary Science Letters, v. 301, p. 479–492, doi:10.1016/j.epsl.2010.11.024.

Arnórsson, S., 1995, Geothermal systems in Iceland: structure and conceptual models—I. High-temperature areas: Geothermics, v. 24, p. 564–602, doi:10.1016/0375-6505(95)00025-9.

Aspinall, W., Auker, M., Hincks, T., Mahony, S., Nadim, F., Pooley, J., Sparks, R.S.J., and Syre, E., 2011, Volcano hazard and exposure in GFDRR priority countries and risk mitigation measures, *in* Volcano Risk Study 0100806–00–1-R: Washington, D.C., Global Facility for Disaster Reduction and Recovery.

Bendick, R., Bilham, R., Asfaw, L., and Klemperer, S., 2006, Distributed Nubia-Somalia relative motion and dyke intrusion in the main Ethiopian rift: Geophysical Journal International, v. 165, p. 303–310, doi:10.1111/j.1365-246X.2006.02904.x.

Benvenuti, M., Carnicelli, S., Belluomini, G., Dainelli, N., Di Grazia, S., Ferrari, G., Iasio, C., Sagri, M., Ventra, D., and Atnafu, B., 2002, The Ziway-Shala lake basin (main Ethiopian rift, Ethiopia): A revision of basin evolution with special reference to the late Quaternary: Journal of African Earth Sciences, v. 35, p. 247–269, doi:10.1016/S0899-5362(02)00036-2.

Benvenuti, M., Bonini, M., Tassi, F., Corti, G., Sani, F., Agostini, A., Manetti, P., and Vaselli, O., 2013, Holocene lacustrine fluctuations and deep CO_2 degassing in the northeastern Lake Langano Basin (Main Ethiopian Rift): Journal of African Earth Sciences, v. 77, p. 1–10, doi:10.1016/j.jafrearsci.2012.09.001.

Beutel, E., van Wijk, J., Ebinger, C., Keir, D., and Agostini, A., 2010, Formation and stability of magmatic segments in the Main Ethiopian and Afar rifts: Earth and Planetary Science Letters, v. 293, p. 225–235, doi:10.1016/j.epsl.2010.02.006.

Biggs, J., Bastow, I.D., Keir, D., and Lewi, E., 2011, Pulses of deformation reveal frequently recurring shallow magmatic activity beneath the Main Ethiopian Rift: Geochemistry, Geophysics, Geosystems, v. 12, p. 1–11, doi:10.1029/2011GC003662.

Boccaletti, M., Bonini, M., Mazzuoli, R., and Abebe, B., 1998, Quaternary oblique extensional tectonics in the Ethiopian Rift (Horn of Africa): Tectonophysics, v. 287, p. 97–116, doi:10.1016/S0040-1951(98)80063-2.

Bonini, M., Corti, G., Fabrizio, I., Manetti, P., Mazzarini, F., Abebe, T., and Pecskay, Z., 2005, Evolution of the Main Ethiopian Rift in the frame of Afar and Kenya rifts propagation: Tectonics, v. 24, TC1007, doi:10.1029/2004TC001680.

Bosworth, W., Burke, K., and Strecker, M., 2003, Effect of stress fields on magma chamber stability and the formation of collapse calderas: Tectonics, v. 22, p. 1042, doi:10.1029/2002TC001369.

Burton, M.R., Sawyer, G.M., and Granieri, D., 2013, Deep carbon emissions from volcanoes, *in* Hazen, R., et al., eds., Carbon in Earth: Reviews in Mineralogy and Geochemistry Volume 75, p. 323–354, doi:10.2138/rmg.2013.75.11.

Caliro, S., Chiodini, G., Galluzzo, D., Granieri, D., La Rocca, M., Saccorotti, G., and Ventura, G., 2005, Recent activity of Nisyros volcano (Greece) inferred from structural, geochemical and seismological data: Bulletin of Volcanology, v. 67, p. 358–369, doi:10.1007/s00445-004-0381-7.

Carapezza, M.L., and Granieri, D., 2004, CO_2 soil flux at Vulcano (Italy): Comparison between active and passive methods: Applied Geochemistry, v. 19, p. 73–88, doi:10.1016/S0883-2927(03)00111-2.

Cardellini, C., Chiodini, G., and Frondini, F., 2003, Application of stochastic simulation to CO_2 flux from soil: Mapping and quantification of gas release: Journal of Geophysical Research, v. 108, p. 2425–2437, doi:10.1029/2002JB002165.

Casey, M., Ebinger, C., Keir, D., Gloaguen, R., and Mohamed, F., 2006, Strain accommodation in transitional rifts: Extension by magma intrusion and faulting in Ethiopian rift magmatic segments, *in* Yirgu, G., et al., eds., The Afar Volcanic Province within the East African Rift System: Geological Society of London Special Publication 259, p. 143–163, doi:10.1144/GSL.SP.2006.259.01.13.

Cashman, K.V., Soule, S.A., Mackey, B.H., Deligne, N.I., Deardorff, N.D., and Dietterich, H.R., 2013, How lava flows: New insights from applications of lidar technologies to lava flow studies: Geosphere, v. 9, p. 1664–1680, doi:10.1130/GES00706.1.

Cebriá, J.M., Martín-Escorza, C., López-Ruiz, J., Morán-Zenteno, D.J., and Martiny, B.M., 2011, Numerical recognition of alignments in monogenetic volcanic areas: Examples from the Michoacán-Guanajuato Volcanic Field in Mexico and Calatrava in Spain: Journal of Volcanology and Geothermal Research, v. 201, p. 73–82, doi:10.1016/j.jvolgeores.2010.07.016.

Chiodini, G., Cioni, R., Guidi, M., and Raco, B., 1998, Soil CO_2 flux measurements in volcanic and geothermal areas: Applied Geochemistry, v. 13, p. 543–552, doi:10.1016/S0883-2927(97)00076-0.

Chiodini, G., Frondini, F., Cardellini, C., Granieri, D., Marini, L., and Ventura, G., 2001, CO_2 degassing and energy release at Solfatra volcano, Campi Flegrei, Italy: Journal of Geophysics, v. 106, p. 16,213–16,221, doi:10.1029/2001JB000246.

Chiodini, G., Avino, R., Brombach, T., Caliro, S., Cardellini, C., De Vita, S., Frondini, F., Granirei, D., Marotta, E., and Ventura, G., 2004, Fumarolic and diffuse soil degassing west of Mount Epomeo, Ischia, Italy: Journal of Volcanology and Geothermal Research, v. 133, p. 291–309, doi:10.1016/S0377-0273(03)00403-7.

Chorowicz, J., Collet, B., Bonavia, F.F., and Korme, T., 1994, Northwest to north-northwest extension direction in the Ethiopian rift deduced from the orientation of extension structures and fault-slip analysis: Geological Society of America Bulletin, v. 106, p. 1560–1570, doi:10.1130/0016-7606(1994)105<1560:NTNNED>2.3.CO;2.

Civetta, L., Cornette, Y., Gillot, P.Y., and Orsi, G., 1988, The eruptive history of Pantelleria (Sicily Channel) in the last 50 ka: Bulletin of Volcanology, v. 50, p. 47–57, doi:10.1007/BF01047508.

Cole, J.W., 1969, Gariboldi Volcanic Complex, Ethiopia: Bulletin Volcanologique, v. 33, p. 566–578, doi:10.1007/BF02596525.

Cole, J.W., Milner, D., and Spinks, K., 2005, Calderas and caldera structures: A review: Earth-Science Reviews, v. 69, p. 1–26, doi:10.1016/j.earscirev.2004.06.004.

Corti, G., 2008, Control of rift obliquity on the evolution and segmentation of the main Ethiopian rift: Nature Geoscience, v. 1, p. 258–262, doi:10.1038/ngeo160.

Corti, G., 2009, Continental rift evolution: From rift initiation to incipient break-up in the Main Ethiopian Rift, East Africa: Earth-Science Reviews, v. 96, p. 1–53, doi:10.1016/j.earscirev.2009.06.005.

Corti, G., Philippon, M., Sani, F., Keir, D., and Kidane, T., 2013a, Re-orientation of the extension direction and pure extensional faulting at oblique rift margins: Comparison between the Main Ethiopian Rift and laboratory experiments: Terra Nova, v. 25, p. 396–404, doi:10.1111/ter.12049.

Corti, G., Sani, F., Philippon, M., Sokoutis, D., Willingshofer, E., and Molin, P., 2013b, Quaternary volcano-tectonic activity in the Soddo region, western margin of the Southern Main Ethiopian Rift: Tectonics, v. 32, p. 1–19, doi:10.1002/tect.20052.

Crowley, J., and Zimbelman, D., 1997, Mapping hydrothermally altered rocks on Mount Rainier, Washington, with airborne visible/infrared imaging spectrometer (AVIRIS) data: Geology, v. 25, p. 559–562, doi:10.1130/0091-7613(1997)025<0559:MHAROM>2.3.CO;2.

Curewitz, D., and Karson, J.A., 1997, Structural settings of hydrothermal outflow: Fracture permeability maintained by fault propagation and interaction: Journal of Volcanology and Geothermal Research, v. 79, p. 149–168, doi:10.1016/S0377-0273(97)00027-9.

Cole, J.W., 1969, Gariboldi Volcanic Complex, Ethiopia: Bulletin Volcanologique, v. 33, p. 566–578, doi:10.1007/BF02596525.

Dakin, G., and Gibson, I.L., 1971, A preliminary account of Alutu, a pantelleritic volcano in the Main Ethiopian Rift: Addis Ababa University Geophysical Observatory Bulletin, v. 13, p. 110–114.

D'Alessandro, W., Brusca, L., Kyriakopoulos, K., Michas, G., and Papadakis, G., 2008, Methana, the westernmost active volcanic system of the south Aegean arc (Greece): Insight from fluids geochemistry: Journal of Volcanology and Geothermal Research, v. 178, p. 818–828, doi:10.1016/j.jvolgeores.2008.09.014.

Darling, W., Gizaw, B., and Arusei, M., 1996, Lake-groundwater relationships and fluid-rock interaction in the East African Rift Valley: Isotopic evidence: Journal of African Earth Sciences, v. 22, p. 423–431, doi:10.1016/0899-5362(96)00026-7.

Di Paola, G.M., 1971, Geology of the Corbetti Caldera area (Main Ethiopian Rift Valley): Bulletin Volcanologique, v. 35, p. 497–506, doi:10.1007/BF02596970.

Di Paola, G.M., 1972, The Ethiopian Rift Valley (between 7°00′ and 8°40′ lat north): Bulletin Volcanologique, v. 36, p. 517–560, doi:10.1007/BF02599823.

Deutsch, C.V., and Journel, A.G., 1998, GSLIB, Geostatistical Software Library and Users Guide: New York, Oxford University Press, 369 p.

Ebinger, C., 2005, Continental break-up: The East African perspective: Astronomy & Geophysics, v. 46, p. 16–21, doi:10.1111/j.1468-4004.2005.46216.x.

Ebinger, C., and Casey, M., 2001, Continental breakup in magmatic provinces: An Ethiopian example: Geol-

ogy, v. 29, p. 527–530, doi:10.1130/0091-7613(2001)029<0527:CBIMPA>2.0.CO;2.

Ebinger, C., Ayele, A., Keir, D., Rowland, J., Yirgu, G., Wright, T., Belachew, M., and Hamling, I., 2010, Length and timescales of rift faulting and magma intrusion: The Afar rifting cycle from 2005 to present: Annual Review of Earth and Planetary Sciences, v. 38, p. 439–466, doi:10.1146/annurev-earth-040809-152333.

ELC Electroconsult, 1986, Exploitation of Aluto-Langano geothermal resources feasibility report, Geothermal Exploration Project, Ethiopian Lake District Rift: Milan, Italy, ELC Electroconsult, 289 p.

Favara, R., Giammanco, S., Inguaggiato, S., and Pecoraino, G., 2001, Preliminary estimate of CO_2 output from Pantelleria Island volcano (Sicily, Italy): Evidence of active mantle degassing: Applied Geochemistry, v. 16, p. 883–894, doi:10.1016/S0883-2927(00)00055-X.

Ferguson, D.J., Maclennan, J., Bastow, I.D., Pyle, D.M., Jones, S.M., Keir, D., Blundy, J.D., Plank, T., and Yirgu, G., 2013, Melting during late stage rifting in Afar is hot and deep: Nature, v. 499, p. 70–73, doi:10.1038/nature12292.

Fink, J., 1980, Surface folding and viscosity of rhyolite flows: Geology, v. 8, p. 250–254, doi:10.1130/0091-7613(1980)8<250:SFAVOR>2.0.CO;2.

Fridriksson, T., Kristjánsson, B.R., Ármannsson, H., Margrétardóttir, E., Ólafsdóttir, S., and Chiodini, G., 2006, CO_2 emissions and heat flow through soil, fumaroles, and steam heated mud pools at the Reykjanes geothermal area, SW Iceland: Applied Geochemistry, v. 21, p. 1551–1569, doi:10.1016/j.apgeochem.2006.04.006.

Frondini, F., Chiodini, G., Caliro, S., Cardellini, C., Granieri, D., and Ventura, G., 2004, Diffuse CO_2 degassing at Vesuvio, Italy: Bulletin of Volcanology, v. 66, p. 642–651, doi:10.1007/s00445-004-0346-x.

Gasse, E., and Street, F., 1978, Late Quaternary lake-level fluctuations and environments of the northern Rift Valley and Afar region (Ethiopia and Djibouti): Palaeogeography, Palaeoclimatology, Palaeoecology, v. 24, p. 279–325, doi:10.1016/0031-0182(78)90011-1.

Gebregzabher, Z., 1986, Hydrothermal alteration minerals in Aluto Langano geothermal wells, Ethiopia: Geothermics, v. 15, p. 735–740, doi:10.1016/0375-6505(86)90086-6.

Geyer, A., and Marti, J., 2008, The new worldwide collapse caldera database (CCDB): A tool for studying and understanding caldera processes: Journal of Volcanology and Geothermal Research, v. 175, p. 334–354, doi:10.1016/j.jvolgeores.2008.03.017.

Giammanco, S., Parello, F., Gambardella, B., Schifano, R., Pizzullo, S., and Galante, G., 2007, Focused and diffuse effluxes of CO_2 from mud volcanoes and mofettes south of Mt. Etna (Italy): Journal of Volcanology and Geothermal Research, v. 165, p. 46–63, doi:10.1016/j.jvolgeores.2007.04.010.

Giammanco, S., Immè, G., Mangano, G., Morelli, D., and Neri, M., 2009, Comparison between different methodologies for detecting radon in soil along an active fault: The case of the Pernicana fault system, Mt. Etna (Italy): Applied Radiation and Isotopes, v. 67, p. 178–185, doi:10.1016/j.apradiso.2008.09.007.

Gianelli, G., and Teklemariam, M., 1993, Water-rock interaction processes in the Aluto-Langano geothermal field (Ethiopia): Journal of Volcanology and Geothermal Research, v. 56, p. 429–445, doi:10.1016/0377-0273(93)90007-E.

Gibert, E., Travi, Y., Massault, M., Tiercelin, J.-J., and Chernet, T., 2002, AMS-^{14}C chronology of a lacustrine sequence from Lake Langano (Main Ethiopian Rift): Correction and validation steps in relation with volcanism, lake water and carbon: Radiocarbon, v. 44, p. 75–92.

Gibson, I.L., 1969, The structure and volcanic geology of an axial portion of the Main Ethiopian Rift: Tectonophysics, v. 8, p. 561–565, doi:10.1016/0040-1951(69)90054-7.

Gibson, I., 1970, A pantelleritic welded ash-flow tuff from the Ethiopian Rift Valley: Contributions to Mineralogy and Petrology, v. 28, p. 89–111, doi:10.1007/BF00404992.

Gillespie, R., Street-Perrott, F., and Switsur, R., 1983, Postglacial arid episodes in Ethiopia have implications for climate prediction: Nature, v. 306, p. 680–683, doi:10.1038/306680a0.

Gizaw, B., 1993, Aluto-Langano geothermal field, Ethiopian Rift Valley: Physical characteristics and the effects of gas on well performance: Geothermics, v. 22, p. 101–116, doi:10.1016/0375-6505(93)90050-W.

Gregg, T.K.P., Fink, J.H., and Griffiths, R.W., 1998, Formation of multiple fold generations on lava flow surfaces: Influence of strain rate, cooling rate, and lava composition: Journal of Volcanology and Geothermal Research, v. 80, p. 281–292, doi:10.1016/S0377-0273(97)00048-6.

Grove, A.T., and Goudie, S., 1971, Late Quaternary lake levels in the rift valley of southern Ethiopia and elsewhere in tropical Africa: Nature, v. 234, p. 403–405, doi:10.1038/234403a0.

Grove, A.T., Street, F.A., and Goudie, S., 1975, Former lake levels and climatic change in the Rift Valley of southern Ethiopia: Geographical Journal, v. 141, p. 177–194, doi:10.2307/1797205.

Hayward, N., and Ebinger, C., 1996, Variations in the along-axis segmentation of the Afar Rift system: Tectonics, v. 15, p. 244–257, doi:10.1029/95TC02292.

Hernández, P., Pérez, N., Salazar, J., Nakai, S., Notsu, K., and Wakita, H., 1998, Diffuse emission of carbon dioxide, methane, and helium-3 from Teide Volcano, Tenerife, Canary Islands: Geophysical Research Letters, v. 25, p. 3311–3314, doi:10.1029/98GL02561.

Hernández, P., Salazar, J., Shimoike, Y., Mori, T., Notsu, K., and Perez, N., 2001, Diffuse emission of CO_2 from Miyakejima volcano, Japan: Chemical Geology, v. 177, p. 175–185, doi:10.1016/S0009-2541(00)00390-9.

Hernández Perez, P., Notsu, K., Tsurumi, M., Mori, T., Ohno, M., Shimoike, Y., Salazar, J., and Perez, N., 2003, Carbon dioxide emissions from soils at Hakkoda, north Japan: Journal of Geophysical Research, v. 108, 2210, doi:10.1029/2002JB001847.

Holohan, E., Troll, V.R., Walter, T.R., Munn, S., McDonnell, S., and Shipton, Z., 2005, Elliptical calderas in active tectonic settings: An experimental approach: Journal of Volcanology and Geothermal Research, v. 144, p. 119–136, doi:10.1016/j.jvolgeores.2004.11.020.

Kebede, S., Mamo, T., and Abebe, T., 1985, Geological report and explanation to the geological map of Aluto-Langano geothermal area: Addis Ababa, Ethiopian Institute of Geological Surveys, 60 p.

Keir, D., Kendall, J.-M., Ebinger, C.J., and Stuart, G.W., 2005, Variations in late syn-rift melt alignment inferred from shear-wave splitting in crustal earthquakes beneath the Ethiopian rift: Geophysical Research Letters, v. 32, L23308, doi:10.1029/2005GL024150.

Keir, D., Ebinger, C.J., Stuart, G.W., Daly, E., and Ayele, A., 2006, Strain accommodation by magmatism and faulting as rifting proceeds to breakup: Seismicity of the northern Ethiopian rift: Journal of Geophysical Research, v. 111, p. 1–17, doi:10.1029/2005JB003748.

Kendall, J., Stuart, G., Ebinger, C., Bastow, I., and Keir, D., 2005, Magma-assisted rifting in Ethiopia: Nature, v. 433, p. 146–148, doi:10.1038/nature03161.

Keranen, K., and Klemperer, S.L., 2008, Discontinuous and diachronous evolution of the Main Ethiopian Rift: Implications for development of continental rifts: Earth and Planetary Science Letters, v. 265, p. 96–111, doi:10.1016/j.epsl.2007.09.038.

Keranen, K., Klemperer, S.L., and Gloaguen, R., 2004, Three-dimensional seismic imaging of a protoridge axis in the Main Ethiopian rift: Geology, v. 32, p. 949–952, doi:10.1130/G20737.1.

Koepenick, K., Brantley, S., Thompson, J., Rowe, G., Nyblade, A., and Moshy, C., 1996, Volatile emissions from the crater and flank of Oldoinyo Lengai volcano, Tanzania: Journal of Geophysical Research, v. 101, p. 13,819–13,830, doi:10.1029/96JB00173.

Lan, T.F., Yang, T.F., Lee, H.-F., Chen, Y.-G., Chen, C.-H., Song, S.-R., and Tsao, S., 2007, Compositions and flux of soil gas in Liu-Huang-Ku hydrothermal area, northern Taiwan: Journal of Volcanology and Geothermal Research, v. 165, p. 32–45, doi:10.1016/j.jvolgeores.2007.04.015.

Le Turdu, C., and 18 others, 1999, The Ziway-Shala lake basin system, Main Ethiopian Rift: Influence of volcanism, tectonics, and climatic forcing on basin formation and sedimentation: Palaeogeography, Palaeoclimatology, Palaeoecology, v. 150, p. 135–177, doi:10.1016/S0031-0182(98)00220-X.

Lipman, P.W., 1997, Subsidence of ash-flow calderas: Relation to caldera size and magma-chamber geometry: Bulletin of Volcanology, v. 59, p. 198–218, doi:10.1007/s004450050186.

Lutz, T., 1986, An analysis of the orientations of large-scale crustal structures: A statistical approach based on areal distributions of pointlike features: Journal of Geophysical Research, v. 91, p. 421–434, doi:10.1029/JB091iB01p00421.

Lutz, T., and Gutmann, J., 1995, An improved method for determining and characterizing alignments of point-like features and its implications for the Pinacate volcanic field, Sonora, Mexico: Journal of Geophysical Research, v. 100, p. 17,659–17,670, doi:10.1029/95JB01058.

Mackenzie, G.D., Thybo, H., and Maguire, P.K.H., 2005, Crustal velocity structure across the Main Ethiopian Rift: Results from two-dimensional wide-angle seismic modelling: Geophysical Journal International, v. 162, p. 994–1006, doi:10.1111/j.1365-246X.2005.02710.x.

Mahood, G.A., 1984, Pyroclastic rocks and calderas associated with strongly peralkaline magmatism: Journal of Geophysical Research, v. 89, 8540, doi:10.1029/JB089iB10p08540.

Mahood, G.A., and Hildreth, W., 1983, Nested calderas and trapdoor uplift at Pantelleria, Strait of Sicily: Geology, v. 11, p. 722–726, doi:10.1130/0091-7613(1983)11<722:NCATUA>2.0.CO;2.

Mahood, G.A., and Hildreth, W., 1986, Geology of the peralkaline volcano at Pantelleria, Strait of Sicily: Bulletin of Volcanology, v. 48, p. 143–172, doi:10.1007/BF01046548.

Mamo, T., 1985, Petrography and rock chemistry of well LA-8 Aluto-Langano geothermal system, Ethiopia: Auckland, New Zealand, University of Auckland Geothermal Institute, 48 p.

Mielnick, P., and Dugas, W., 2000, Soil CO_2 flux in a tallgrass prairie: Soil Biology & Biochemistry, v. 32, p. 221–228, doi:10.1016/S0038-0717(99)00150-9.

Mohr, P., 1966, Chabbi volcano (Ethiopia): Bulletin of Volcanology, v. 29, p. 797–815, doi:10.1007/BF02597195.

Mohr, P., Mitchell, J.G., and Raynolds, R.G.H., 1980, Quaternary volcanism and faulting at O'A caldera, central Ethiopian rift: Bulletin of Volcanology, v. 43, p. 173–189, doi:10.1007/BF02597619.

Nakamura, K., 1977, Volcanoes as possible indicators of tectonic stress orientation—Principle and proposal: Journal of Volcanology and Geothermal Research, v. 2, p. 1–16, doi:10.1016/0377-0273(77)90012-9.

Neave, D.A., Fabbro, G., Herd, R.A., Petrone, C.M., and Edmonds, M., 2012, Melting, differentiation and degassing at the Pantelleria volcano, Italy: Journal of Petrology, v. 53, p. 637–663, doi:10.1093/petrology/egr074.

Notsu, K., Sugiyama, K., Hosoe, M., Uemura, A., Shimoike, Y., Tsunomori, F., Sumino, H., Yamamoto, J., Mori, T., and Hernández, P., 2005, Diffuse CO_2 efflux from Iwojima volcano, Izu-Ogasawara arc, Japan: Journal of Volcanology and Geothermal Research, v. 139, p. 147–161, doi:10.1016/j.jvolgeores.2004.08.003.

Padrón, E., Hernández, P., Toulkeridis, T., Pérez, N.M., Marrero, R., Melián, G., Virgili, G., and Notsu, K., 2008, Diffuse CO_2 emission rate from Pululahua and the lake-filled Cuicocha calderas, Ecuador: Journal of Volcanology and Geothermal Research, v. 176, p. 163–169, doi:10.1016/j.jvolgeores.2007.11.023.

Pantaleo, M., and Walter, T.R., 2013, The ring-shaped thermal field of Stefanos crater, Nisyros Island: A conceptual model: Solid Earth Discussions, v. 5, p. 2005–2042, doi:10.5194/sed-5-2005-2013.

Parkinson, K., 1981, An improved method for measuring soil respiration in the field: Journal of Applied Ecology, v. 18, p. 221–228, doi:10.2307/2402491.

Parks, M.M., Caliro, S., Chiodini, G., Pyle, D.M., Mather, T.A., Berlo, K., Edmonds, M., Biggs, J., Nomikou, P., and Raptakis, C., 2013, Distinguishing contributions to diffuse CO_2 emissions in volcanic areas from magma degassing and thermal decarbonation using soil gas

$^{222}Rn–\delta^{13}C$ systematics: Application to Santorini volcano: Earth and Planetary Science Letters, v. 377–378, p. 180–190, doi:10.1016/j.epsl.2013.06.046.

Paulsen, T.S., and Wilson, T.J., 2010, New criteria for systematic mapping and reliability assessment of monogenetic volcanic vent alignments and elongate volcanic vents for crustal stress analyses: Tectonophysics, v. 482, p. 16–28, doi:10.1016/j.tecto.2009.08.025.

Peccerillo, A., Barberio, M.R., Yirgu, G., Ayalew, D., Barbieri, M., and Wu, T.W., 2003, Relationships between mafic and peralkaline silicic magmatism in continental rift settings: A petrological, geochemical and isotopic study of the Gedemsa Volcano, Central Ethiopian Rift: Journal of Petrology, v. 44, p. 2003–2032, doi:10.1093/petrology/egg068.

Peltier, A., Finizola, A., Douillet, G.A., Brothelande, E., and Garaebiti, E., 2012, Structure of an active volcano associated with a resurgent block inferred from thermal mapping: The Yasur–Yenkahe volcanic complex (Vanuatu): Journal of Volcanology and Geothermal Research, v. 243–244, p. 59–68, doi:10.1016/j.jvolgeores.2012.06.022.

Pizzi, A., Coltorti, M., Abebe, B., Disperati, L., Sacchi, G., and Salvini, R., 2006, The Wonji fault belt (Main Ethiopian Rift): structural and geomorphological constraints and GPS monitoring, *in* Yirgu, G., et al., eds., The Afar Volcanic Province within the East African Rift System: Geological Society of London Special Publication 259, p. 191–207, doi:10.1144/GSL.SP.2006.259.01.16.

Pyle, D.M., and Elliott, J.R., 2006, Quantitative morphology, recent evolution, and future activity of the Kameni Islands volcano, Santorini, Greece: Geosphere, v. 2, p. 253–268, doi:10.1130/GES00028.1.

Rampey, M.L., Oppenheimer, C., Pyle, D.M., and Yirgu, G., 2010, Caldera-forming eruptions of the Quaternary Kone Volcanic Complex, Ethiopia: Journal of African Earth Sciences, v. 58, p. 51–66, doi:10.1016/j.jafrearsci.2010.01.008.

Rampey, M.L., Oppenheimer, C., Pyle, D.M., and Yirgu, G., 2014, Physical volcanology of the Gubisa Formation, Kone Volcanic Complex, Ethiopia: Journal of African Earth Sciences, v. 96, p. 212–219, doi:10.1016/j.jafrearsci.2014.04.009.

Remy, N., Boucher, A., and Wu, J., 2009, Applied Geostatistics with SGeMS, A User's Guide: Cambridge, United Kingdom, Cambridge University Press, 284 p.

Rey, A., Pegoraro, E., Tedeschi, V., De Parri, I., Jarvis, P.G., and Valentini, R., 2002, Annual variation in soil respiration and its components in a coppice oak forest in central Italy: Global Change Biology, v. 8, p. 851–866, doi:10.1046/j.1365-2486.2002.00521.x.

Rowland, J.V., and Sibson, R.H., 2004, Structural controls on hydrothermal flow in a segmented rift system, Taupo Volcanic Zone, New Zealand: Geofluids, v. 4, p. 259–283, doi:10.1111/j.1468-8123.2004.00091.x.

Saibi, H., Aboud, E., and Ehara, S., 2012, Analysis and interpretation of gravity data from the Alutо-Langano geothermal field of Ethiopia: Acta Geophysica, v. 60, p. 318–336, doi:10.2478/s11600-011-0061-x.

Salazar, J.M.L., Hernández, P.a., Pérez, N.M., Melián, G., Álvarez, J., Segura, F., and Notsu, K., 2001, Diffuse emission of carbon dioxide from Cerro Negro Volcano, Nicaragua, Central America: Geophysical Research Letters, v. 28, p. 4275–4278, doi:10.1029/2001GL013709.

Schöpa, A., Pantaleo, M., and Walter, T.R., 2011, Scale-dependent location of hydrothermal vents: Stress field models and infrared field observations on the Fossa Cone, Vulcano Island, Italy: Journal of Volcanology and Geothermal Research, v. 203, p. 133–145, doi:10.1016/j.jvolgeores.2011.03.008.

Shimoike, Y., Kazahaya, K., and Shinohara, H., 2002, Soil gas emission of volcanic CO_2 at Satsuma-Iwojima volcano, Japan: Earth, Planets, and Space, v. 54, p. 239–247, doi:10.1186/BF03353023.

Siebert, L., and Simkin, T., 2002, Volcanoes of the world: An illustrated catalog of Holocene volcanoes and their eruptions: Smithsonian Institution, Global Volcanism Program Digital Information Series, GVP-3 (www.volcano.si.edu/gvp/world/).

Siniscalchi, A., Tripaldi, S., Neri, M., Giammanco, S., Piscitelli, S., Balasco, M., Behncke, B., Magrì, C., Naudet, V., and Rizzo, E., 2010, Insights into fluid circulation across the Pernicana Fault (Mt. Etna, Italy) and implications for flank instability: Journal of Volcanology and Geothermal Research, v. 193, p. 137–142, doi:10.1016/j.jvolgeores.2010.03.013.

Stamps, D.S., Calais, E., Saria, E., Hartnady, C., Nocquet, J.-M., Ebinger, C.J., and Fernandes, R.M., 2008, A kinematic model for the East African Rift: Geophysical Research Letters, v. 35, L05304, doi:10.1029/2007GL032781.

Street, F., 1979, Quaternary lakes in the Ziway-Shala Basin, southern Ethiopia [Ph.D. thesis]: Cambridge, UK, University of Cambridge, 475 p.

Teklemariam, M., 1996, Water-rock interaction processes in the Aluto-Langano geothermal field Ethiopia [Ph.D. thesis]: Pisa, Italy, University of Pisa, 245 p.

Teklemariam, M., Battaglia, S., Gianelli, G., and Ruggieri, G., 1996, Hydrothermal alteration in the Aluto-Langano geothermal field, Ethiopia: Geothermics, v. 25, p. 679–702, doi:10.1016/S0375-6505(96)00019-3.

Tibaldi, A., 1995, Morphology of pyroclastic cones and tectonics: Journal of Geophysical Research, v. 100, p. 24,521–24,535, doi:10.1029/95JB02250.

Trippanera, D., Porreca, M., Ruch, J., Pimentel, A., Acocella, V., Pacheco, J., and Salvatore, M., 2014, Relationships between tectonics and magmatism in a transtensive/transform setting: An example from Faial Island (Azores, Portugal): Geological Society of America Bulletin, v. 126, p. 164–181, doi:10.1130/B30758.1.

Valori, A.M., Teklemariam, M., and Ginaelli, G., 1992, Evidence of temperature increase of CO_2-bearing fluids from Aluto-Langano geothermal field (Ethiopia): A fluid inclusions study of deep wells LA-3 and LA-6: European Journal of Mineralogy, v. 4, p. 907–920, doi:10.1127/ejm/4/5/0907.

Vasco, D.W., Puskas, C.M., Smith, R.B., and Meertens, C.M., 2007, Crustal deformation and source models of the Yellowstone volcanic field from geodetic data: Journal of Geophysical Research, v. 112, B07402, doi:10.1029/2006JB004641.

Viveiros, F., Cardellini, C., Ferreira, T., Caliro, S., Chiodini, G., and Silva, C., 2010, Soil CO_2 emissions at Furnas volcano, São Miguel Island, Azores archipelago: Volcano monitoring perspectives, geomorphologic studies, and land use planning application: Journal of Geophysical Research, v. 115, B12208, doi:10.1029/2010JB007555.

Wadge, G., and Cross, A., 1988, Quantitative methods for detecting aligned points: An application to the volcanic vents of the Michoacan-Guanajuato volcanic field, Mexico: Geology, v. 16, p. 815–818, doi:10.1130/0091-7613(1988)016<0815:QMFDAP>2.3.CO;2.

Werner, C., and Cardellini, C., 2006, Comparison of carbon dioxide/ emissions with fluid upflow, chemistry, and geologic structures at the Rotorua geothermal system, New Zealand: Geothermics, v. 35, p. 221–238, doi:10.1016/j.geothermics.2006.02.006.

Werner, C., Brantley, S.L., and Boomer, K., 2000, CO_2 emissions related to the Yellowstone volcanic system: 2. Statistical sampling, total degassing, and transport mechanisms: Journal of Geophysical Research, v. 105, 10831, doi:10.1029/1999JB900331.

Werner, C., Hurwitz, S., Evans, W.C., Lowenstern, J.B., Bergfeld, D., Heasler, H., Jaworowski, C., and Hunt, A., 2008, Volatile emissions and gas geochemistry of Hot Spring Basin, Yellowstone National Park, USA: Journal of Volcanology and Geothermal Research, v. 178, p. 751–762, doi:10.1016/j.jvolgeores.2008.09.016.

White, J.C., Parker, D.F., and Ren, M., 2009, The origin of trachyte and pantellerite from Pantelleria, Italy: Insights from major element, trace element, and thermodynamic modelling: Journal of Volcanology and Geothermal Research, v. 179, p. 33–55, doi:10.1016/j.jvolgeores.2008.10.007.

Williams, R., Branney, M.J., and Barry, T.L., 2013, Temporal and spatial evolution of a waxing then waning catastrophic density current revealed by chemical mapping: Geology, v. 42, p. 107–110, doi:10.1130/G34830.1.

Wilson, C.J.N., Rogan, A.M., Smith, I.E.M., Northey, D.J., Nairn, I.A., and Houghton, B.F., 1984, Caldera volcanoes of the Taupo Volcanic Zone, New Zealand: Journal of Geophysical Research, v. 89, p. 8463–8484, doi:10.1029/JB089iB10p08463.

Woldegabriel, G., Aronson, J.L., and Walter, R.C., 1990, Geology, geochronology, and rift basin development in the central sector of the Main Ethiopia Rift: Geological Society of America Bulletin, v. 102, p. 439–458, doi:10.1130/0016-7606(1990)102<0439:GGARBD>2.3.CO;2.

Wolfenden, E., Ebinger, C., Yirgu, G., Deino, A., and Ayalew, D., 2004, Evolution of the northern Main Ethiopian rift: Birth of a triple junction: Earth and Planetary Science Letters, v. 224, p. 213–228, doi:10.1016/j.epsl.2004.04.022.

Yimer, M., 1984, The petrogenesis, chemistry and hydrothermal mineralogy of rocks in the Langano-Aluto geothermal system, Ethiopia: Auckland, New Zealand, University of Auckland Geothermal Institute, 75 p.